

Recent Progress and Challenges in Mixed Ionic–Electronic Conducting Membranes for Oxygen Separation

Young-il Kwon, Gyeong Duk Nam, Gahyeon Lee, Soomin Choi, and Jong Hoon Joo*

Carbon neutrality refers to the state of making net-zero emissions of carbon dioxide (CO₂), which is a key concept in tackling global warming. It can be achieved by offsetting carbon emissions as well as balancing reduced and emitted emissions. Globally, CO₂ is emitted mainly from fossil fuel power plants. The use of carbon capture and storage technology, including pre-, post-, and oxy-fuel combustion capture, in power plants can provide a carbon-neutral strategy that allows for the sustainable use of fossil fuels while potentially reducing CO₂ emissions. Oxy-fuel combustion capture facilitates CO₂ capture by simplifying combustion products through the reaction of recirculated flue gas with a high-purity oxygen. Oxygen transport membranes, which produce pure oxygen by oxygen transport via oxides at high temperatures, have attracted increased interest because they can improve overall efficiency when integrated with oxy-fuel combustion capture. Dual-phase membranes with fluorite structure have greater potential for commercialization than perovskite-based single-phase membranes, which have poor chemical and mechanical properties. However, despite these advantages, their low oxygen permeability remains a critical issue. This review focuses on progress in the development of dual-phase membranes and summarizes various approaches that can facilitate bulk diffusion and surface exchange, which affect the oxygen permeability.

1. Introduction


As the climate crisis caused by atmospheric carbon dioxide has become a serious issue worldwide, efforts to realize carbon neutrality are being strongly promoted, mainly in developed countries. Globally, most CO₂ is emitted primarily from fossil fuel

power plants. If pure oxygen rather than air is supplied as fuel for the power plants, the capture and storage of CO₂ can be advantageous because the amount of nitric oxide (NO_x) in the exhausted flue gas can be minimized. Facilities capable of producing several thousand tons of oxygen daily and sufficient electricity are required to implement oxy-combustion in these power plants.^[1] Because the cost of constructing and maintaining an oxygen production facility strongly affects the cost of CO₂ recovery, more efficient oxygen production technology is as important as technology for CO₂ capture by oxygen combustion. Currently, the only commercialized high-capacity oxygen production technology is a cryogenic process that compresses, cools, and expands air to produce liquid oxygen. However, the cryogenic method is energy-intensive, which is approximately 15% of the electricity generated by coal power generation. Thus, alternative methods of oxygen production are needed. A mixed ionic and electronic conductor (MIEC)-based oxygen transport membrane

(OTM) that can produce high-purity oxygen with higher energy efficiency than energy-intensive cryogenic distillation technology is receiving considerable attention.^[2,3] The oxygen transport membrane is a ceramic separator that operates at a high temperature ($\geq 700^\circ\text{C}$). If a difference in oxygen partial pressure is maintained across the separator, only oxygen is selectively transported, and oxygen can be produced. Because oxygen is separated by electrochemical permeation through vacancies in the lattice of an MIEC membrane, the selectivity is theoretically infinite. This innovative oxygen transport membrane technology can significantly reduce production costs compared to those of the conventional cryogenic process. Additionally, this new technology enables process intensification that can significantly improve the process and energy efficiency by integrating several reaction processes in addition to pure oxygen production.^[4–6] Many studies have been conducted to support the industrialization of oxygen separation membranes, ranging from basic research such as permeability and stability studies to applied research on modularization. In particular, dual-phase membranes composed of stable ionic and electronic conductors have attracted substantial attention for the commercialization of oxygen transport membranes.^[7,8] These membranes can overcome the drawbacks of single-phase membranes composed of perovskite oxide, which have low chemical and mechanical stability under the operating

G. D. Nam, G. Lee, S. Choi, J. H. Joo
School of Earth Sciences and Environmental Engineering
Gwangju Institute of Science and Technology
Gwangju 61005, Republic of Korea
E-mail: jhjoo@gist.ac.kr

Y. Kwon
Department of Urban, Energy, and Environmental Engineering
Chungbuk National University
Cheongju, Chungbuk 28644, Republic of Korea

 The ORCID identification number(s) for the author(s) of this article can be found under <https://doi.org/10.1002/aesr.202200086>.

© 2022 The Authors. Advanced Energy and Sustainability Research published by Wiley-VCH GmbH. This is an open access article under the terms of the Creative Commons Attribution License, which permits use, distribution and reproduction in any medium, provided the original work is properly cited.

DOI: 10.1002/aesr.202200086

conditions. However, despite the advantages of the dual-phase membranes, their low oxygen permeability compared to single-phase membranes remains a challenge. Several excellent reviews have discussed recent progress in membrane research from various perspectives.^[3,9–12] However, methods of improving the permeability in terms of surface exchange and bulk diffusion, which dominate oxygen permeation through the membrane, have not been reviewed in detail. The permeability of oxygen transport membranes is not determined solely by the intrinsic properties (e.g., oxygen ionic conductivity) of the materials; structural properties such as membrane thickness can also play a crucial role in enhancing the oxygen permeation flux.^[13] Thus, to obtain industrial levels of oxygen flux, it is essential not only to improve the material properties but also to decrease the membrane thickness. The oxygen permeation flux is typically controlled by both bulk diffusion and surface exchange.^[14,15] If the membrane is thick enough that the effect of surface exchange is negligible, oxygen permeation occurs only by bulk diffusion. By contrast, with decreasing membrane thickness, the permeability is dominated by surface exchange.

Thus, to improve the oxygen permeability toward the commercialization of oxygen transport membranes, surface exchange and bulk diffusion should be considered simultaneously. This review focuses on progress in the development of dual-phase membranes in the last decade, highlighting various approaches that can promote the bulk diffusion and surface exchange rates in oxygen separation membranes using various materials and structures.

1.1. Types of Oxygen Transport Membrane

Depending on the material applied for the ambipolar diffusion of oxygen ions and electrons, oxygen transport membranes are typically classified as single-phase or dual-phase membranes, as shown in **Figure 1**. Most single-phase membranes were developed using perovskite oxides with mainly electronic conductivity, such as $\text{Ba}_{0.5}\text{Sr}_{0.5}\text{Co}_{0.8}\text{Fe}_{0.2}\text{O}_{3-\delta}$ and $\text{La}_{0.6}\text{Sr}_{0.4}\text{Co}_{0.2}\text{Fe}_{0.8}\text{O}_{3-\delta}$ (LSCF), which have attracted much attention in terms of ensuring high oxygen permeability.^[16,17] However, the industrial application of single-phase membranes is limited because of the trade-off relationship between stability and oxygen permeability. Most of the perovskite oxides used in single-phase membranes

contain alkaline-earth ions with high basicity; thus, they may form carbonate in an atmosphere containing CO_2 .^[18,19] Their practical application still faces many problems, such as unsatisfactory mechanical and thermomechanical stability as well as poor chemical stability in the presence of CO_2 .^[20,21] Because oxygen transport membranes operate at elevated temperatures, excellent thermomechanical stability is required. However, the high thermal expansion coefficient (TEC) ($>20 \times 10^{-6} \text{ K}^{-1}$)^[22] and poor mechanical stability of perovskite result in delamination or cracking of the membrane at elevated temperatures. To address this problem, dual-phase membranes with fluorite structure, which affords intrinsic high mechanical and chemical stability as an ionic conductor, have been intensively studied to improve the overall stability and oxygen permeability. The reason is that the fluorite oxides used as the electrolyte in a solid oxide fuel cell (SOFC) are mechanically and chemically stable under the membrane operating conditions.^[19,23] However, because the bulk diffusion and surface exchange kinetics of materials having fluorite structure materials are typically sluggish than those of perovskite oxides, the addition of the fluorite oxides to the dual-phase membrane generally decreases the oxygen permeation flux.^[24,25] Sufficient mechanical and chemical stability for industrial use can be ensured by using a dual-phase membrane; however, the low oxygen permeability of dual-phase membranes is still below the commercial level ($J_{\text{O}_2} = 5\text{--}10 \text{ mL min}^{-1} \text{ cm}^{-2}$).^[26] Thus, in this review, we describe various approaches to the industrial application of dual-phase membranes considering surface exchange and bulk diffusion.

1.2. Permeation Mechanism of Oxygen Transport Membranes

The mechanism of oxygen permeation through a membrane typically comprises surface exchange and bulk diffusion, as shown in **Figure 2a**. Bulk diffusion occurs by oxygen-ion transfer through oxygen vacancies in the lattice, and surface exchange involves multiple steps, including oxygen adsorption, dissociation, and reduction at the surface. When oxygen permeation through a membrane is controlled by bulk diffusion, and the membrane is thick enough to be unaffected by surface exchange, the oxygen flux obeys the Wagner equation^[27]

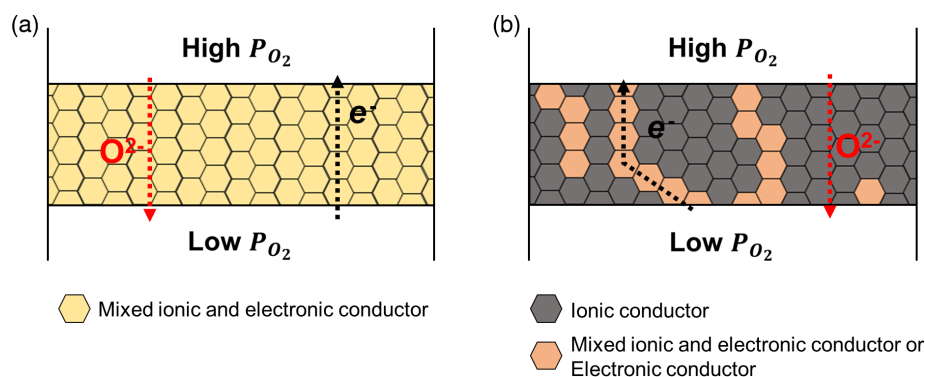


Figure 1. Schematic of the type of the oxygen transport membrane: a) single-phase membrane and b) dual-phase membrane.

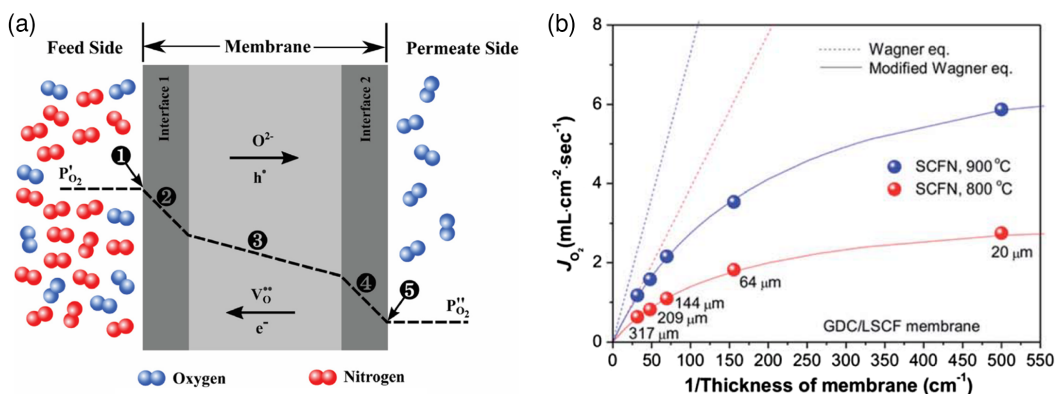


Figure 2. a) Oxygen transport mechanism through membrane. Reproduced with permission.^[12] Copyright 2018, Elsevier. b) Oxygen permeation flux of the SCFN-coated fluorite-rich dual-phase membrane as a function of the inverse of the thickness membrane at 900 and 800 °C. Reproduced with permission.^[7] Copyright 2020, Royal Society of Chemistry.

$$J_{O_2} = -\frac{RT}{16F^2L} \int_{\ln P_{O_2}^{\text{high}}}^{\ln P_{O_2}^{\text{low}}} \frac{\sigma_{\text{ion}}\sigma_{\text{el}}}{\sigma_{\text{ion}} + \sigma_{\text{el}}} d \ln P_{O_2} \quad (1)$$

where J_{O_2} (mol cm⁻² s⁻¹) denotes the oxygen flux, L (cm) is the membrane thickness, σ_{el} (S cm⁻¹) is the electronic conductivity, σ_{ion} (S cm⁻¹) is the ionic and electronic conductivity, R (J mol⁻¹ K⁻¹) is the gas constant, T (K) is the temperature, F (C mol⁻¹) is the Faraday constant, and $P_{O_2}^{\text{high}}$ (atm) and $P_{O_2}^{\text{low}}$ (atm) are the oxygen partial pressures on the feed and permeate sides of the membrane, respectively. Because the conductivity of the electronic conducting phase in dual-phase membranes that use electronic percolation is typically at least several times higher than that of the oxygen-ion-conducting phase, the ambipolar conductivity ($\sigma_{\text{ion}}\sigma_{\text{el}}/\sigma_{\text{ion}} + \sigma_{\text{el}}$) of the membranes can be represented by the ionic conductivity. According to the Wagner equation, decreasing the membrane thickness can enhance the oxygen permeation flux. However, as the membrane becomes thinner, surface exchange becomes the rate-determining step in oxygen permeation, where the oxygen flux is limited by both bulk diffusion and surface exchange. When both processes are considered, the oxygen permeation can be described by the following modified Wagner equation,^[28] as shown in Figure 2b.

$$J_{O_2} = -\frac{1}{1 + (2L_c/L)} \frac{RT}{16F^2L} \int_{\ln P_{O_2}^{\text{high}}}^{\ln P_{O_2}^{\text{low}}} \sigma_{\text{ion}} d \ln P_{O_2} \quad (2)$$

where L_c is the characteristic thickness and can be expressed as

$$L_c = \frac{D_s}{k_s} = \frac{D^*}{k_s} \quad (3)$$

where k_s denotes the surface exchange coefficient at the gas–solid interface, D_s is the self-diffusion coefficient of oxygen ions, and D^* is the tracer diffusion coefficient. When the correlation effect is negligible, D^* can be assumed to be equal to D_s . Note that L_c is

a function of the process parameters and not the intrinsic properties of the material, as both the surface exchange and diffusion coefficients depend on temperature and oxygen partial pressure. L_c is defined as the thickness at which oxygen permeation becomes controlled mainly by surface exchange instead of bulk diffusion. That is, the maximum achievable oxygen permeability can be expected when the thickness is very close to zero, and the permeation can then be written as $1/2J_{\text{ex}}^{\text{total}}$.^[29] Therefore, if the exchange coefficient cannot be significantly increased for thicknesses of less than L_c under the experimental conditions, the permeability cannot be significantly improved by decreasing the membrane thickness.

2. Studies of Dual-Phase Membranes Considering Bulk Diffusion of Oxygen Ions

2.1. Electrical Percolation Limit of Dual-Phase Membranes

To optimize oxygen permeation through dual-phase membranes, good percolation by two continuously distributed ionic and electronic conducting phases must be obtained. Thus, the maximum oxygen permeability can be expected when the content of the ion-conducting phase is maximum in the range in which the electronic conducting phase is sufficient. Dual-phase membranes are typically designed as a composite of 60–80 vol% ionic conductor and 20–40 vol% electronic conductor. However, the percolation limit of dual-phase membranes is affected not only by the electronic conductivity of the material but also by the size, shape, and distribution of the constituents. To determine the electronic percolation threshold, the general effective media (GEM) equation can be applied when the conductivities of the two phases constituting the dual-phase membrane differ significantly.^[14,15]

$$\frac{f(\sigma_f^{1/t} - \sigma_{\text{tot}}^{1/t})}{\sigma_f^{1/t} + (f_c/(1 - f_c))\sigma_{\text{tot}}^{1/t}} + \frac{(1 - f)(\sigma_p^{1/t} - \sigma_{\text{tot}}^{1/t})}{\sigma_p^{1/t} + (f_c/(1 - f_c))\sigma_{\text{tot}}^{1/t}} = 0 \quad (4)$$

Here, f_c , f , and t are the critical (percolation) volume fraction of the perovskite phase, volume fraction of the perovskite phase, and exponent of percolation, respectively; σ_f , σ_p , and

σ_{tot} represent the conductivities of fluorite, perovskite, and the composite, respectively. Thus, by inserting the experimental data into the GEM equation, the percolation limit of a dual-phase membrane can be accurately determined by estimating the values of f_c and t .^[30,31]

To maximize the fraction of the ionic conducting phase by reducing the percolation limit of the electronic conducting phase in dual-phase membranes, Chen et al.^[32] designed a $\text{Ce}_{0.8}\text{Sm}_{0.2}\text{O}_{2-\delta}$ - $\text{PrBaCo}_2\text{O}_{5+\delta}$ (SDC-PBCO) membrane with a special microstructure in which the electronic conducting phase had a fiber-like shape (Figure 3a). Consequently, the electrical percolation limit was reduced by 20%, and the oxygen permeability at 900 °C was approximately twice that of a 60 vol% SDC-40 vol% PBCO membrane. Zeng et al.^[33] performed detailed characterization and quantification of a $\text{Ce}_{0.8}\text{Gd}_{0.2}\text{O}_{2-\delta}$ - FeCo_2O_4 (GDC-FCO) dual-phase membrane according to the phase and microstructure (Figure 3b). They found that if the grain sizes of all phases in the dual-phase membrane are similar, the optimal ambipolar conductivity is obtained when the volume ratio of the ionic and electronic conductors is close to 4:1.

2.2. Ionic Conductors for the Dual-Phase Membranes

The main charge carrier in ionic conductors, which have negligible electron conduction by electrons and holes, is the oxygen ion. The ionic conductors most commonly used in dual-phase membranes are fluorite oxides with AO_2 structure. In the fluorite structure (Figure 4), the A-site contains large tetravalent cations such as Zr^{4+} and Ce^{4+} , which occupy the regular sites in the face-centered cubic structure. Oxygen anions in the fluorite structure are coordinated to the eight tetrahedral interstitial sites. Among fluorite oxides, ZrO_2 , Bi_2O_3 , and CeO_2 have been studied for application as ionic conductors in dual-phase membranes.

ZrO_2 is characterized by phase changes as a function of temperature. Pure ZrO_2 is in the monoclinic phase at room temperature. However, the structure changes to the tetragonal phase at 1170 °C and to cubic crystal structure at 2300 °C.^[34,35] The phase transition from monoclinic to tetragonal is accompanied by a considerable volume change ($\approx 5\%$), which interferes with the sintering of ZrO_2 .^[36] In particular, ZrO_2 in the cubic phase is of great interest because it has higher ionic conductivity than the monoclinic phase.^[37] Thus, to obtain high ionic conductivity

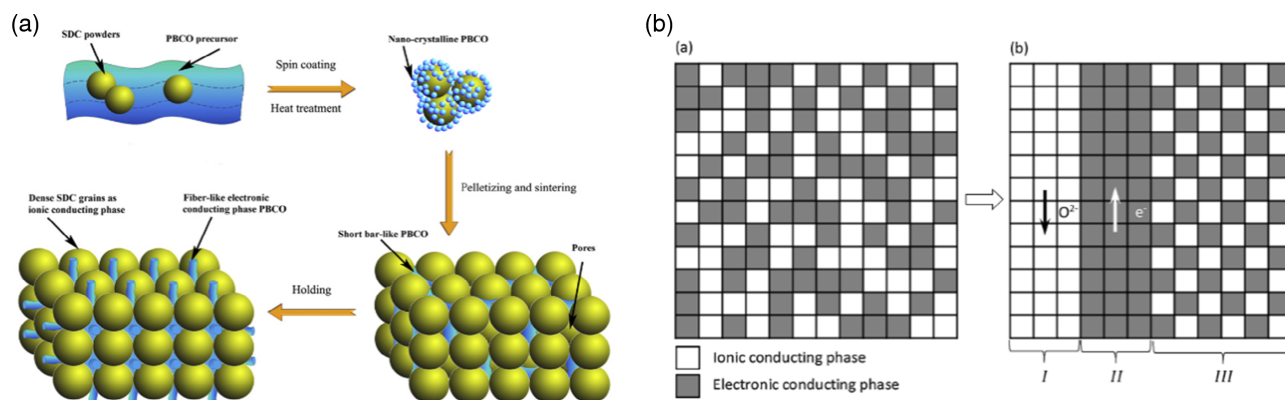


Figure 3. a) Schematic illustration of the novel strategy for the synthesis of SDC-PBCO membrane with fiber-like PBCO phase distributing in the matrix of SDC phase. Reproduced with permission.^[32] Copyright 2013, Elsevier. b) A microscopic schematic diagram of a randomly distributed dual-phase oxygen transport membrane. Reproduced with permission.^[33] Copyright 2020, Elsevier.

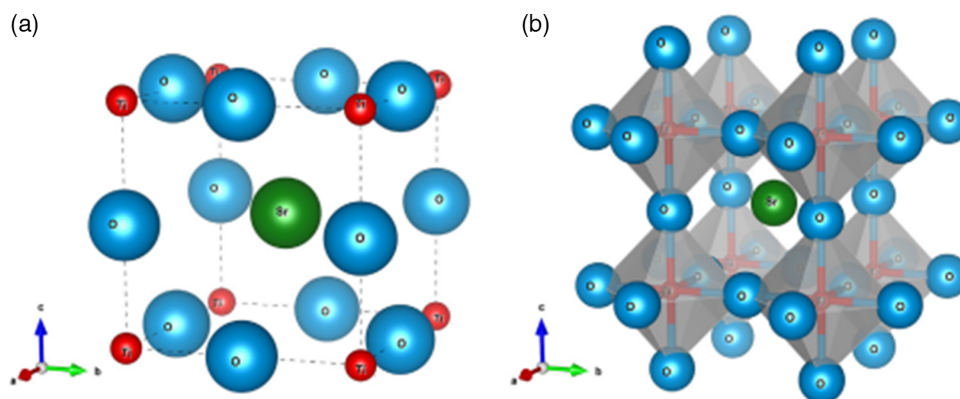


Figure 4. a) Crystal structure and b) packing arrangement of an ideal AO_2 fluorite compound exemplified by CaF_2 (blue spheres—A (Ca) cation; red spheres—O (F) anion). Reproduced with permission.^[12] Copyright 2018, Elsevier.

and eliminate mechanical stress due to the volume change by maintaining the cubic phase of ZrO_2 at room temperature, dopants such as Y_2O_3 , MgO , and CaO can be added to pure ZrO_2 .^[38] Furthermore, the addition of a dopant with a valence lower than that of the host cation forms oxygen vacancies for charge compensation, which improves the oxygen ion conductivity.



However, because of steric blocking by large cations, the addition of dopant cations with a larger ionic radius than the host cation (Zr^{4+}) can not only hinder the migration of oxygen vacancies but also result in high activation energy and low conductivity.^[39–41] Thus, the highest ionic conductivity is expected to be obtained using a dopant cation having an ionic radius similar to that of Zr^{4+} . The ionic radius of Sc^{3+} is most similar to that of Zr^{4+} , followed by those of Yb , Y , Gd , and Nd (Figure 5).^[40]

In the binary ZrO_2 – Sc_2O_3 system, when more than 10 mol% of Sc_2O_3 is doped into ZrO_2 , Sc_2O_3 -stabilized ZrO_2 is in the cubic phase at high temperature and the rhombohedral phase below approximately 500 °C.^[42] Because the rhombohedral phase is less conductive than the cubic phase, doping with up to 10 mol% Sc_2O_3 is appropriate for maintaining high ionic conductivity. Despite the high ionic conductivity and phase stability of Sc_2O_3 -doped ZrO_2 , the high cost of scandium and decrease in the ionic conductivity of ScSZ during annealing at elevated temperature make it less attractive for the commercialization of dual-phase membranes.^[43,44] Thus, to solve these commercialization problems, Y_2O_3 -stabilized ZrO_2 (YSZ), in which ZrO_2 is doped with yttrium instead of scandium, has been widely studied. At low doping levels, the ionic conductivity generally increases linearly with dopant content. However, there is a threshold above which the ionic conductivity decreases with increasing doping level because of an association between oxygen vacancies and the formation of dopant cations: $[\text{M}'_{\text{Zr}} - \text{V}_{\text{O}}^{\bullet\bullet}]$ or $[\text{M}'_{\text{Zr}} - \text{V}_{\text{O}}^{\bullet\bullet} - \text{M}'_{\text{Zr}}]^{\times}$. Thus, for YSZ, when ZrO_2 is doped with

8 mol% Y_2O_3 , the maximum ionic conductivity of 0.03 S cm^{-1} is obtained at 850 °C.^[45]

Most zirconia-based dual-phase membranes reported in the past decade contain YSZ or ScSZ as the ionic conductor. However, the oxygen permeability of zirconia-based membranes is lower than expected despite the high ionic conductivities of ScSZ and YSZ. The reason is secondary phase formation during sintering, which is among the most frequently mentioned problems with zirconia-based membranes. During the sintering of zirconia-based membranes, secondary phases such as $\text{La}_2\text{Zr}_2\text{O}_7$ and SrZrO_3 form because of the interdiffusion of zirconium with rare- and alkaline-earth metals (La, Sr), which hinders oxygen ion transport and thus decreases the oxygen permeability.^[8] Therefore, to use stabilized zirconia as an ionic conductor for dual-phase membranes, it is necessary to minimize the formation of secondary phases with the electronic conductor during sintering.

Doped CeO_2 is considered a promising ionic conductor for dual-phase membranes because its ionic conductivity at intermediate temperatures is higher than that of stabilized zirconia. In addition, regardless of whether CeO_2 is doped with other oxides, it has a stable cubic fluorite structure up to its melting point. Although pure CeO_2 has extremely low oxygen ionic conductivity, oxygen vacancies can be introduced, as in ZrO_2 , by doping with a dopant having a lower valence than that of the host cation (Ce^{4+}), which enhances the oxygen ionic conductivity.



The conductivity of doped CeO_2 shows a similar dependence to that of stabilized ZrO_2 on the ionic radius and doping level of the dopant. Therefore, the highest oxygen ionic conductivity is obtained by doping with Sm^{3+} , which has the most similar ionic radius to Ce^{4+} ; the dopants Gd , Dy , Y , and Nd also increase the ionic conductivity, in decreasing order (Figure 6).^[46] However, unlike stabilized ZrO_2 , CeO_2 tends to exhibit electronic conductivity due to the formation of polarons in a reducing atmosphere.^[47,48] Oxygen is released as a gas from the CeO_2 lattice

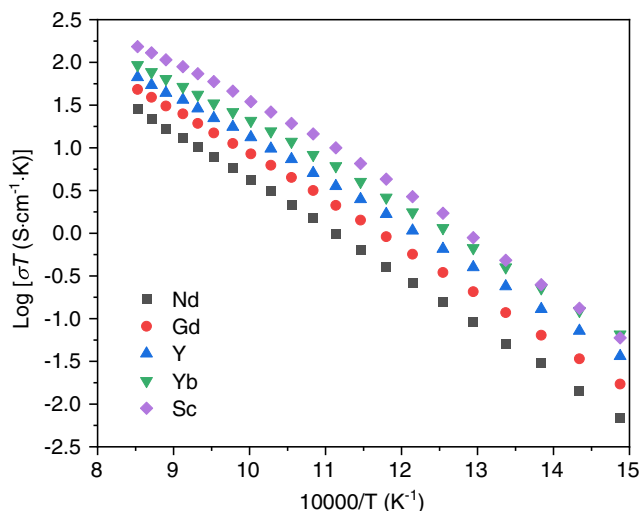


Figure 5. Arrhenius plots for the $\text{Zr}_{0.75}\text{Ce}_{0.08}\text{M}_{0.17}\text{O}_{1.92}$ compositions. Reproduced with permission.^[40] Copyright 2002, Elsevier.

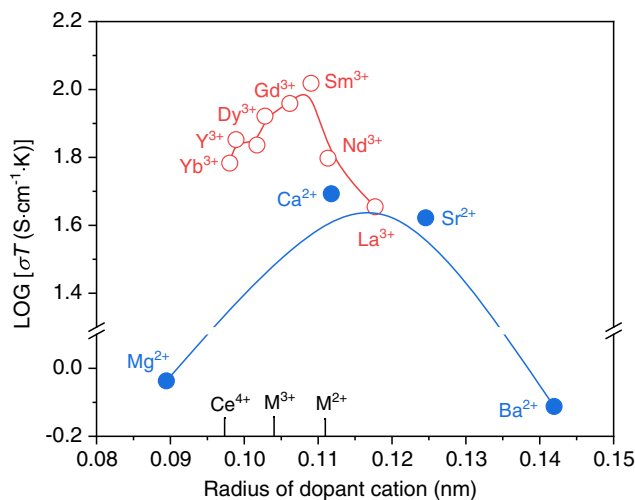


Figure 6. Ionic conductivity of doped ceria at 1073 K against the radius of dopant cation. Reproduced with permission.^[46] Copyright 1996, Elsevier.

under high-temperature reducing conditions, forming oxygen vacancies. As a result of charge compensation for these oxygen vacancies, excess electrons are generated as follows.



These electrons reduce the valence of Ce from Ce^{+4} to Ce^{+3} , causing CeO_2 to have mixed ionic and electronic conductivity. This reduction in the valence of Ce also causes unexpected chemical expansion. Thus, these phenomena can limit its application in reactors operating in a reducing atmosphere.

2.3. Electronic Conductors for the Dual-Phase Membranes

The requirements for the electronic conductor in dual-phase membranes vary depending on the application. However, because permeability and stability are essential for commercialization, the following should generally be considered: high stability, high electronic conductivity, excellent chemical compatibility between components, and economy. In the initial stage of development, noble metals (e.g., Au, Ag, Pd, Pt) were used as an electronic conductor.^[49–51] However, considering the permeability efficiency, the volume content of noble metals is generally approximately 20–40%, which greatly reduces the economic feasibility of the membrane. To reduce the high material cost of dual-phase membranes, electronic-conducting oxides have been proposed to replace precious metals. Oxides with various structures, such as perovskite, spinel, and layered perovskite, are used as electronic conductors in dual-phase membrane systems. They can be classified as MIECs and electronic conductors (for those with negligible oxygen ionic conductivity) depending on the type of charge carrier. The use of pure electronic conductors as the electron path in dual-phase membranes based on electronic percolation can reduce the volume ratio of the ionic conducting phase and limit oxygen ion diffusion in the bulk membrane. Consequently, the ionic path of the membrane is adversely affected by the electronic conductor, as shown in **Figure 7a**.^[52] By contrast, the application of MIEC materials as electronic conductors has a positive effect on the oxygen pathways in the membrane (Figure 7b). Fluorite-rich dual-phase membranes using either an MIEC or a pure electronic conductor for electronic percolation were reported recently by Joo et al., for example, a 20 vol % LSCF–80 vol % GDC membrane coated with $\text{La}_{0.6}\text{Sr}_{0.4}\text{CoO}_{3-\delta}$ (LSC64)^[14] and a 20 vol % $\text{La}_{0.7}\text{Sr}_{0.3}\text{MnO}_{3\pm\delta}$ (LSM)–80 vol % GDC membrane using an LSC64 active layer.^[15] The oxygen permeation flux of the LSCF–GDC membrane is much higher than that of the LSM–GDC membrane, indicating that to improve the oxygen permeability, MIECs could be a more suitable electronic conductor for dual-phase membranes. However, MIECs typically have a high TEC; thus, mechanical and thermomechanical instability can result from TEC mismatch with the ionic conductor at elevated temperatures. The problem of instability associated with the ionic conducting phase and TEC mismatch can be simply solved by applying an electronic conducting phase with a low TEC value. However, there are several aspects that should be considered. A direct correlation exists between oxygen ionic conductivity and thermal expansion in perovskite systems, which indicates that oxygen vacancy concentrations have a dominant

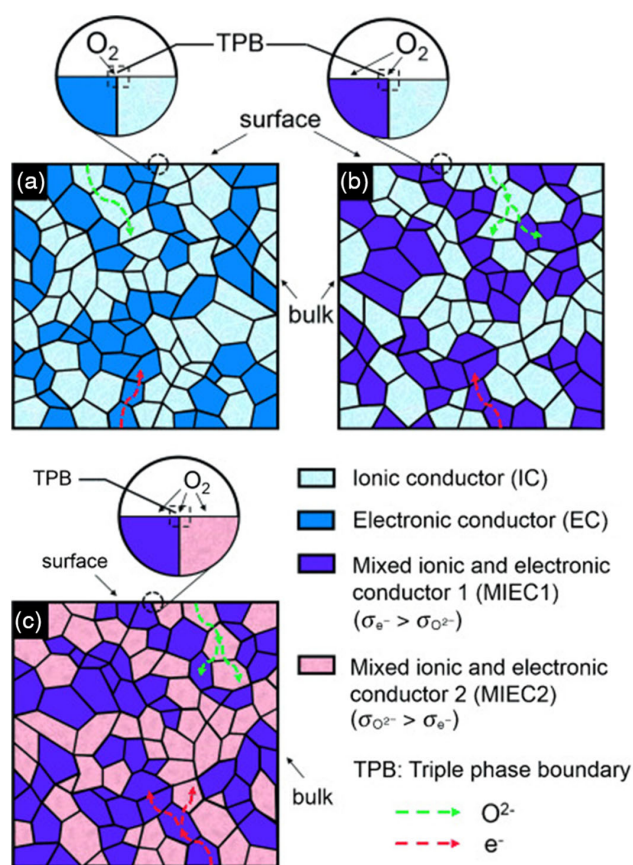


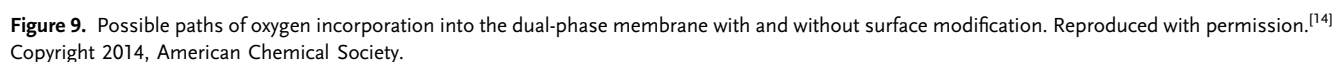
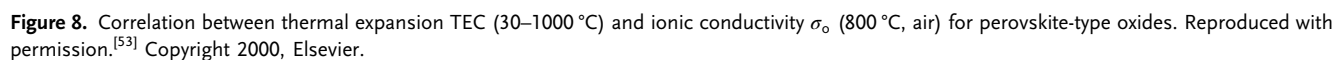
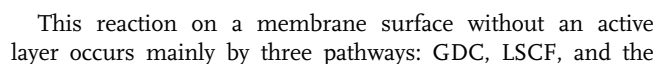
Figure 7. Oxygen ion and electron transport paths of a) electronic conductor–ionic conductor composite membrane and b) mixed ionic and electronic conductor–ionic conductor dual-phase membrane. Reproduced with permission.^[52] Copyright 2015, Wiley-VCH GmbH.

effect on both quantities. The logarithm of the oxygen ionic conductivity and TEC gives the linear relationship, as shown in **Figure 8**,^[53] indicating that there is a trade-off relationship between oxygen permeability and instability originating from TEC mismatch in the fluorite-rich dual-phase membrane.

3. Studies of Surface Exchange in Dual-Phase Membranes

3.1. Permeation Mechanism in Dual-Phase Membranes with Active Layer

Methods of improving the permeability of dual-phase membranes with low oxygen permeability compared to single-phase membranes have been studied for several decades. The use of an active layer has been considered as a representative method to enhance the oxygen permeation flux. Joo et al.^[14] explained the effect of the active layer on flux enhancement in dual-phase membranes and suggested possible pathways for incorporating oxygen into a fluorite-rich dual-phase membrane (80 vol % GDC–20 vol % LSCF) with or without an LSC active layer, as schematically shown in **Figure 9**. The incorporation of gaseous oxygen


$$\text{O}_{\text{ads}}^{2-} + \text{V}_{\text{O}}^{\bullet\bullet} \rightarrow \text{O}_{\text{O}}^{\times} \text{ (Incorporation)} \quad (10)$$


triple-phase boundary between GDC, LSCF, and gaseous oxygen. On the surface of a membrane without an active layer (Figure 9a), oxygen incorporation on the GDC surface (the first path) is expected to be extremely sluggish owing to the low electronic conductivity of GDC. The surface of LSCF (the second path), which is a representative material for single-phase membranes with mixed ionic and electronic conductivity, has high activity for oxygen incorporation. However, in dual-phase membranes, the added LSCF phase has little effect on the permeation. The reason is the very low distribution of percolated LSCF compared to GDC over the entire surface resulting from the low LSCF volume ratio, as well as isolated LSCF, which is inert to oxygen incorporation. Although the activation energy of surface exchange coefficient for LSCF (1.39 eV)^[55] is significantly lower than that of GDC (3.3 eV),^[56] the activation energy of oxygen flux in the dual-phase membrane is affected mainly by that of GDC rather than that of LSCF, assuming that the effect of LSCF on the GDC-rich dual-phase membrane is negligible. In a dual-phase system, high activity for oxygen incorporation typically appears at the triple-phase boundary. However, because the distribution of the triple-phase boundary on the membrane surface depends on the volume ratio of LSCF, it can be deduced that the oxygen permeability of the bare membrane is determined by the GDC phase, as assumed for the second path. On the other hand, there is a study that conflicts with this observation. P. Seeharaj et al.^[57] investigated the surface exchange coefficients of $\text{La}_{0.6}\text{Sr}_{0.4}\text{CoO}_{3-\delta}$ - $\text{Ce}_{0.9}\text{Gd}_{0.1}\text{O}_{2-\delta}$ (20–30 vol% LSC/80–70 vol% GDC) composites using isotope exchange and depth profiling by secondary ion mass spectrometry which is an effective method to obtain the atomistic description of the oxygen transport property in solids. Despite the relatively low volume fraction of LSC in the composites, it was observed that the fast surface exchange on the LSC phase was preserved, as well as the activation energy for the surface exchange coefficient was similar to that of the LSC, suggesting that there is a synergistic effect at the LSC/GDC interface by using GDC supplying the mobile oxygen vacancies and LSC with mixed conductivity supplying electron species for the charge transfer reactions.^[47] As such, conflicting results have been reported in the interpretation of activation energy for oxygen permeability, isotope exchange depth profiling technique results of composites, and further studies are needed to understand the correlation between them. By contrast, on the surface of a membrane with an active layer (Figure 9b), the use of a perovskite-based active layer with high mixed conductivity plays an important role in transferring electrons from the percolated LSCF to the membrane surface. Thus, the active layer can enhance the amount of triple-phase boundary on the surface, which affects oxygen incorporation. Note that the use of an active layer not only increased the oxygen permeability but also changed the activation energy of oxygen flux from 2.76 to 0.64 eV, which is similar to that of the ionic conductivity of GDC (0.61 eV).^[56] In summary, the surface modification of fluorite-based dual-phase membranes using an active layer can enhance the oxygen flux, which is closely related to the change of the rate-limiting step in oxygen permeation from surface exchange to bulk diffusion in the GDC phase. Note that the active layer must have sufficient electronic conductivity, but high electronic conductivity does not ensure high oxygen incorporation. Alder et al.^[58] showed that oxygen incorporation in mixed ionic

and electronic conducting oxides involves the oxygen surface exchange kinetics, vacancy concentration, vacancy diffusivity, and connectivity of the mixed conductor if the mixed conductor has sufficient ion transport. Kwon et al.^[59] experimentally demonstrated that enhanced surface exchange kinetics in the active layer is crucial for improving the oxygen flux in a fluorite-based dual-phase membrane, whereas high electronic conductivity and increased bulk diffusion in the active layer do not significantly improve the permeability.

3.2. Active Layer Materials for Dual-Phase Membrane

The basic concept of oxygen transport membrane can be originated from the electronic and ionic conduction mechanism of electrode and electrolyte in solid oxide electrochemical cells (SOCs). As the oxygen transport membrane can be considered an internal short-circuit SOCs and has an operating principle similar to that of the cathode in SOCs (in particular, the cathode in SOFCs), the materials of the membrane active layer for the oxygen incorporation are generally used interchangeably as SOC cathode materials for the oxygen reduction reaction. Therefore, the active layer material of the membrane must meet the essential criteria for the cathode material of the SOFC: 1) sufficient porosity for the diffusion of gases into the active layer; 2) superior chemical compatibility between the active layer and membrane; 3) high catalytic activity toward oxygen incorporation at the triple-phase boundary; 4) facile ionic and electronic transport in the bulk; and 5) high surface exchange and diffusion coefficients.

3.2.1. Active Layers with Alkaline-Earth Metals

The standard chemical formula of perovskite is ABO_3 , where A and B each donate a distinct cation (Figure 10a).^[60] A typical structure has large 12-coordinated cations at the A site and small 6-coordinated cations at the B site. The ideal structure of perovskite oxides is typically the cubic phase at room temperature. Perovskites have various structures because of the distortion originating from the substitution of cations at the A and B sites, the charge difference between the A and B site cations, the formation of oxygen and cation vacancies, the ionic radii difference between the dopant and host, and variation among the oxygen and cations. Because of the various chemical compositions and structures, perovskite oxides have a wide range of properties (e.g., dielectric properties, electrical conductivity, superconductivity, and catalytic activity). The doping of alkaline-earth metal elements (e.g., Sr, Ca, Ba) may enhance the ionic conductivity and promote the oxygen reduction reaction, which is associated with the oxygen incorporation reaction. The perovskite lanthanum cobaltite (LaCoO_3) is widely used as the cathode in SOCs because of its electrical conductivity and catalytic activity. LaCoO_3 has excellent hole conductivity (as high as 100 S cm^{-1}) and can improve electrical conductivity by increasing the mobile charge carriers produced by charge compensation resulting from partial substitution of aliovalent cations at the A site. Consequently, most of the perovskite oxides considered as active layers for oxygen transport membranes are based on $\text{La}_{1-x}\text{Sr}_x\text{CoO}_3$ (LSC). In the LSC system, the electrical

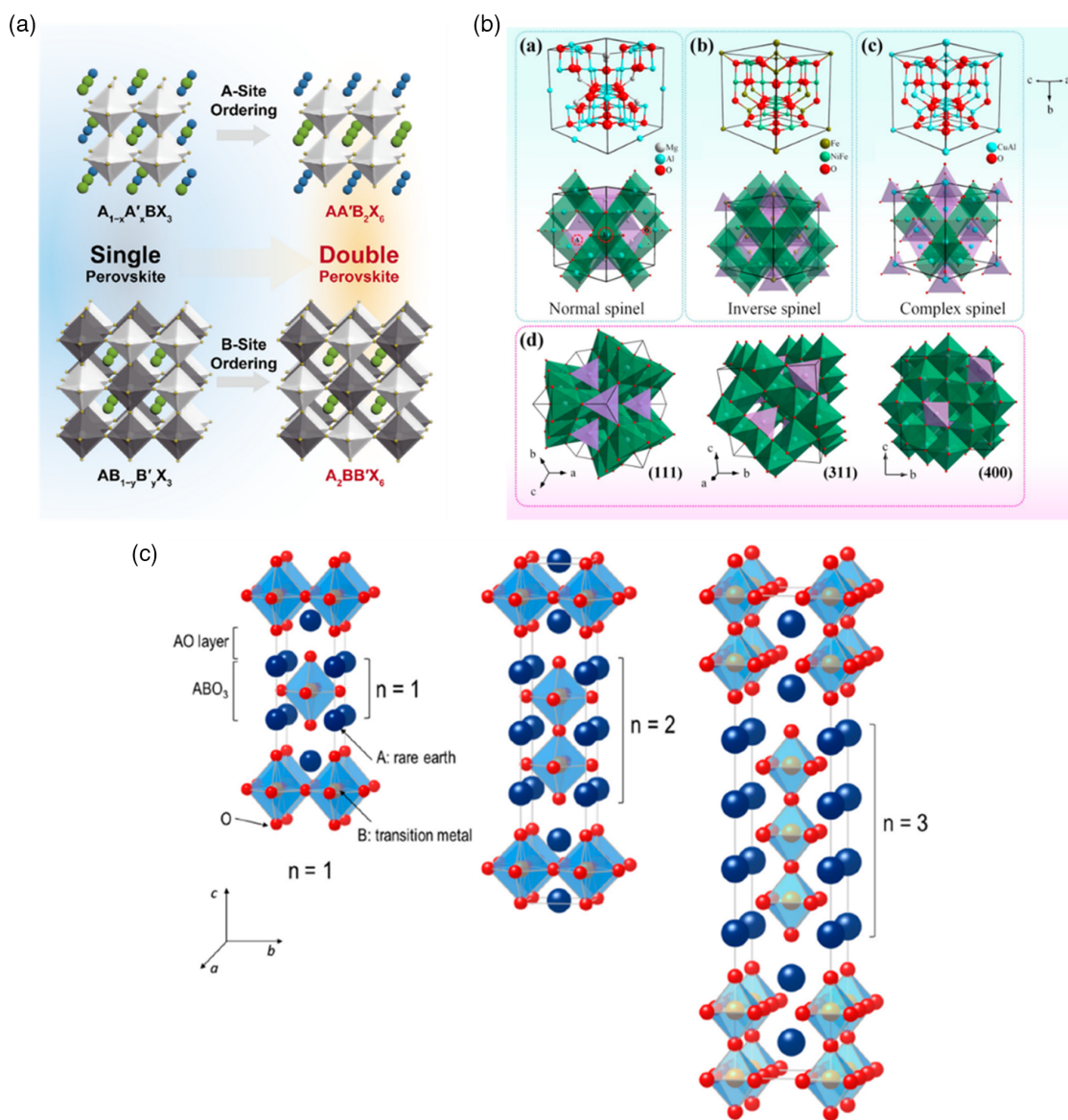


Figure 10. a) A schematic depicting the formation of perovskite and double perovskite. Reproduced with permission.^[60] Copyright 2017, Elsevier. b) Representative structures of a normal spinel ($MgAl_2O_4$), an inverse spinel ($NiFe_2O_4$), and a complex spinel ($CuAl_2O_4$) in different styles and views. Reproduced with permission.^[95] Copyright 2017, American Chemical Society. c) A schematic depicting the ideal tetragonal crystal structure (space group: $I4/mmm$) of Ruddlesden-Popper perovskites, $A_{n+1}B_nX_{3n+1}$ ($n = 1, 2, \text{ and } 3$). Reproduced with permission.^[99] Copyright 2017, MDPI.

conductivity, a crucial property of the cathode, is significantly improved for $x \geq 0.2$ because of the material changes from semi-conducting to the metallic state.^[61] The electrical conductivity commonly increases until $x \approx 0.5$ and then decreases for $x > 0.5$ because of the higher degree of ionic charge compensation.^[62] However, because the TEC of LSC is proportional to the Sr content, the use of LSC with high nonstoichiometry with strontium does not ensure thermomechanical stability due to the delamination and degradation of the electrode resulting from the TEC mismatch between the electrode (TEC of LSC: $19.6 \times 10^{-6} \text{ K}^{-1}$ at 25 to 1000°C)^[63] and the fluorite-based electrolyte (TEC of GDC: $12.8 \times 10^{-6} \text{ K}^{-1}$ at 50 to 1000°C).^[64] Hwang et al.^[65] constructed and tested an SOC using $\text{La}_{1-x}\text{Sr}_x\text{CoO}_{3-\delta}$

cathodes with each composition and suggested the optimal composition by investigating the effect of Sr content on the properties of the $\text{La}_{1-x}\text{Sr}_x\text{CoO}_{3-\delta}$ cathode and overall cell performance. LSC64 is confirmed as the most suitable form of LSC for SOFCs in terms of electrochemical performance. It is the active layer material most commonly used to improve the oxygen permeability of fluorite-rich dual-phase membranes. The use of an LSC64 active layer generally improved the permeability of all membranes,^[14,15,59,66–73] and the thinnest membrane ($\approx 30 \mu\text{m}$), 80 vol% GDC–20 vol% LSCF,^[14] showed the largest increase in permeability. This tendency toward improved oxygen permeability suggests that as the membrane thickness decreases, the surface exchange kinetics becomes dominant. In addition to

LSC, an active layer $\text{SrCo}_{0.1}\text{Fe}_{0.8}\text{Nb}_{0.1}\text{O}_{3-\delta}$ (SCFN) with a higher surface exchange coefficient ($3.47 \times 10^{-5} \text{ cm s}^{-1}$ at 900°C) was used in a fluorite-rich dual-phase membrane having a thickness of $20 \mu\text{m}$ to significantly improve the oxygen permeability. Nam et al. demonstrated that a GDC–LSCF membrane with high oxygen flux and overall stability can be obtained by using an active material having a high CO_2 tolerance and surface exchange coefficient in a fluorite-rich dual-phase membrane.^[7] Niobium-doped strontium cobaltite with a SrCoO_3 perovskite oxide was used as the active layer. The CO_2 resistance was enhanced by doping high-valence Nb at the B site of SCFN because the high oxidation number of Nb improves the acidity of the B site, which maintains time-dependent stability in the CO_2 atmosphere. The doping strategy was suggested to overcome the technical issues associated with LSC materials with even higher TECs than the membranes at high temperatures. In this regard, the importance of partial substitution at the B site as well as A site doping has been discussed; in one of the most promising systems to date, Fe is partially substituted for Co at the B site. Tai et al.^[74,75] conducted practical studies on the significant properties of $\text{La}_{1-x}\text{Sr}_x\text{Co}_{1-y}\text{Fe}_y\text{O}_3$ (LSCF) according to the values of x and y . They investigated the phase transition and Arrhenius behavior of LSCF and characterized its effect on the peak electrical conductivity and thermal expansion; they suggested that $\text{La}_{0.6}\text{Sr}_{0.4}\text{Co}_{0.2}\text{Fe}_{0.8}\text{O}_3$ is the optimal composition for use as an active material. Several studies have reported significantly enhanced permeability by applying LSCF as an active layer in dual-phase membranes such as GDC–FCO^[76], $\text{Ce}_{0.8}\text{Tb}_{0.2}\text{O}_{2-\delta}$ – NiFe_2O_4 (CTO–NFO),^[77,78] and GDC–LSCF.^[59] The thinnest GDC–LSCF membrane, with a thickness of $32 \mu\text{m}$, showed the largest increase in oxygen permeation, indicating that as the membrane thickness decreases, surface exchange affects the oxygen permeability more strongly than bulk diffusion does. Strontium-doped lanthanum manganite ($\text{La}_{1-x}\text{Sr}_x\text{MnO}_{3\pm\delta}$, LSM) with perovskite structure is also considered an attractive cathode material because of its high electronic conductivity. In contrast to LSC and LSCF oxides, LSM has a low TEC ($10.1 \times 10^{-6} \text{ K}^{-1}$ at 25 to 850°C);^[79] thus, excellent chemical stability can be expected when it is used as a cathode material. However, because LSM has very poor oxygen ionic conductivity ($5.9 \times 10^{-7} \text{ S cm}^{-1}$ at 900°C),^[80] it is necessary to improve the ionic conduction before it can be used as a cathode material. To address this issue, its integration with materials having excellent ionic conductivity, such as electrolyte materials, is being studied. In several studies, a composite coating layer ($\text{La}_{0.8}\text{Sr}_{0.2}\text{MnO}_{3\pm\delta}$ –GDC) was applied as an active layer to GDC– $\text{LaCo}_{0.2}\text{Ni}_{0.4}\text{Fe}_{0.4}\text{O}_{3-\delta}$ ^[81] and CTO–NFO^[82,83] membranes. However, an active layer with a high surface exchange coefficient k^* is essential to improve the oxygen permeability, and the LSM–GDC composite active layer did not significantly increase the oxygen flux because of the low surface exchange coefficient (k^* of GDC: $\approx 6.1 \times 10^{-9} \text{ cm s}^{-1}$ at 800°C ^[24] and k^* of LSM: $\approx 2.4 \times 10^{-9} \text{ cm s}^{-1}$ at 800°C ^[84]). The layered perovskites $\text{LnBaCo}_2\text{O}_{5+\delta}$ (where Ln represents a rare-earth element) have received increased attention as active layer materials for dual-phase membranes.^[85] The stacking sequence of CoO_2 – LnO_5 – CoO_2 – BaO – CoO_2 is the ideal structure of this compound, and oxygen vacancies are mainly located in the plane of the LnO_5 rare earth.^[86] This distribution of oxygen vacancies can improve

the oxygen transport properties compared to those of unordered perovskites and provide surface defect sites capable of facilitating reactions with molecular oxygen.^[87] PBCO reportedly has a higher conductivity ($\approx 900 \text{ S cm}^{-1}$ at 500°C) and a faster oxygen surface exchange coefficient (k_{chem} of $10^{-3} \text{ cm s}^{-1}$ at 350°C) and bulk diffusion coefficient (D_{chem} of $10^{-5} \text{ cm}^2 \text{ s}^{-1}$ at 350°C) than other layered $\text{LnBaCo}_2\text{O}_{5+\delta}$ compounds.^[88] Chen et al.^[89] reported that the oxygen flux of a $450 \mu\text{m}$ -thick SDC–PBCO dual-phase membrane was enhanced remarkably by modifying the feed side surface with the membrane itself, which suppressed the chemical incompatibility between the active layer and membrane. However, although strontium doping (e.g., of LSC and LSCF) can accelerate surface exchange related to oxygen incorporation and exocorporation, strontium may degrade the performance degradation because of reactions with contaminants (e.g., H_2O and CO_2) in the operation atmosphere of the membrane. Zhao et al. studied the effects of 5% CO_2 and 2.81% H_2O in the atmosphere on the electrode performance of LSCF at various temperatures.^[90] They found that the formation of a Sr-related carbonate insulating surface layer can dramatically degrade the performance. In terms of the thermodynamics, in an ambient atmosphere containing H_2O and CO_2 , SrCO_3 is thermally decomposed at temperatures above 680°C , indicating that an active layer containing alkaline-earth metal elements substantially affects oxygen permeation during operation below 680°C . Decreasing the operating temperature from 1000 to 500°C can reduce energy consumption by 39%, indicating that the operating temperature of the membrane should be below 700°C for heat integration and enhanced process efficiency in commercial applications.^[91] In summary, the CO_2 tolerance of the active layer under ambient atmosphere is a key factor to be considered for performance improvement, in addition to the electrical conductivity and surface exchange coefficient.

3.2.2. Active Layers without Alkaline-Earth Metals

Because of the drawbacks of active layers containing alkaline-earth metals, several efforts have been made to obtain stable operation. The development of alkaline-earth metals-free active layer material has been considered as an alternative. In the last decade, composite oxide-based active layer materials that do not contain strontium, such as perovskite, spinel, and Ruddlesden–Popper (RP) structures, have been developed and used experimentally in oxygen transport membranes. Spinel oxides have good oxygen reduction reaction activity, high electronic conductivity, chemical stability, and a low TECs,^[92–94] making it a good active layer candidate for oxygen transport membranes. According to the distribution of A and B cations in the interstices between the tetrahedron and octahedron, the $\text{A}_{1-x}\text{B}_x(\text{A}_x\text{B}_{2-x})\text{O}_4$ spinel structure can be classified into three types (Figure 10b): normal ($x = 0$), inverse ($x = 1$), and complex ($0 < x < 1$).^[95–97] The distribution of A and B cations is determined by factors such as the radii of the cations, Coulombic interactions, and crystal field effects. Because of their range of compositions, electron configurations, and valence states, spinel-structured oxides have been used as catalysts, supercapacitors, and SOFC cathode materials. García-Fayos et al.^[98] reported a CTO–NFO dual-phase membrane study using an active layer consisting of a

spinel-fluorite structure composite based on NFO. At 850–700 °C, the oxygen flux increased by a factor of 2–4 after active porous NFO–CTO layers were added on both sides of the dense membrane, and the oxygen flux in CO₂ atmosphere was observed to have time-dependent stability. The RP structure has the general formula A_{n+1}B_nO_{3n+1} and consists of layers of ABO₃ perovskite and AO rock salt sequentially distributed along the *c*-axis.^[99,100] The schematic diagram of the A_{n+1}B_nO_{3n+1} structure in Figure 10c shows that the A site generally contains rare-earth elements or alkaline-earth metal elements, and the B site typically contains transition metals such as Ni, Mn, Cu, and Fe.^[101] The RP structure has high ionic and electronic conductivity and low thermal expansion, which are essential properties for a SOFC cathode. Ionic and electronic conduction in an RP-structured oxide occurs by a redox reaction or a transition metal valence state change at the B site resulting from a difference in valence state between the host and dopant.^[102] Thermal expansion is caused by the formation of oxygen vacancies because of the partial reduction of B site cations.^[103] Many studies have explored materials in which catalytic activity and thermal stability are balanced by controlling this mechanism. Kwon et al.^[8] reported that the oxygen permeation flux of a 70 vol% Zr_{0.79}Sc_{0.2}Ce_{0.01}O_{2-δ}–30 vol% La_{0.7}Sr_{0.3}MnO_{3±δ} (ScSZ–LSM) membrane was significantly improved by adding an active Nd₂NiO_{4+δ} (NNO) layer to both surfaces of the membrane. Further, the membrane coated with an

NNO active layer exhibited a highly stable oxygen permeation flux, even in pure CO₂ atmosphere. Yun et al.^[104] reported that the oxygen flux of a fluorite-rich dual-phase membrane (GDC–LSM) was dramatically improved by modifying both surfaces with a Pr₂NiO_{4+δ} (PNO) material. The membrane also demonstrated remarkable stability under pure CO₂ conditions and thermomechanical stability during rapid thermal cycling.

3.3. Chemical Compatibility at Active Layer/Membrane Interface

As previously stated, because the effect of surface exchange on the permeability becomes dominant with decreasing membrane thickness, it is important to improve the permeability by surface modification. Modifying a dense membrane with a porous active layer with a superior surface exchange coefficient can improve permeability by increasing the number of reaction sites and by facilitating oxygen in-/excorporation reaction. In this process, the interfacial resistance between the active layer and membrane should be minimized. Lee et al. showed improved oxygen flux through a La_{0.7}Sr_{0.3}Ga_{0.6}Fe_{0.4}O_{3-δ} (LSGF) membrane after surface modification using LSC. However, they found that a new phase, for example, (La_{1-x}Sr_x)(Co_yGa_zFe_{1-y-z})O_{3-δ}, was observed at the active layer/membrane interface during the high-temperature manufacturing of the active layers and during operation, which might reduce the long-term stability of the

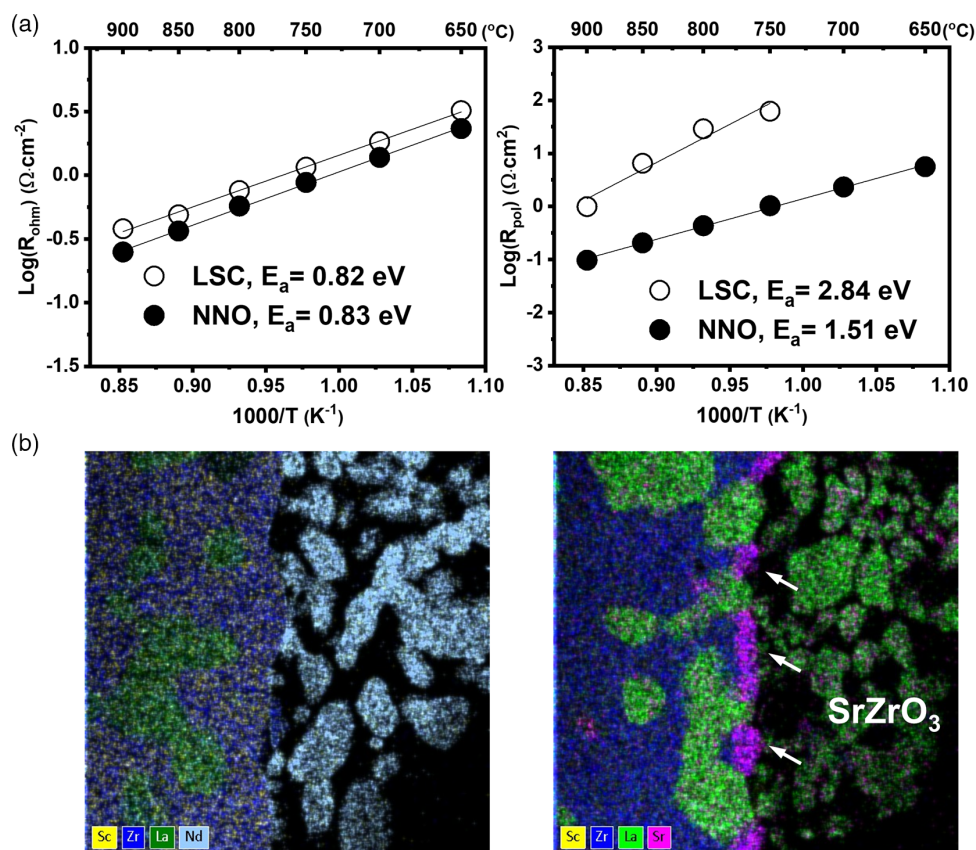


Figure 11. a) Ohmic and polarization resistance as a function of the temperature. b) High resolution-transmission electron microscopy energy-dispersive X-ray spectroscopy (HR-TEM EDS) elemental maps of Zr, Nd, La, and Sr in the vicinity of the Nd₂NiO_{4+δ}/La_{0.7}Sr_{0.3}MnO_{3±δ}–Zr_{0.79}Sc_{0.2}Ce_{0.01}O_{2-δ} membrane and La_{0.6}Sr_{0.4}CoO_{3-δ}/LSM–ScSZ membrane interfaces. Reproduced with permission.^[8] Copyright 2019, Royal Society of Chemistry.

Table 1. Oxygen permeation flux data of various dual-phase membranes reported in the literature.

Nos.	Material	Active layer	Thickness [μm]	Temp. [$^{\circ}\text{C}$]	Flux [$\text{mL cm}^{-2} \text{min}^{-1}$]	P_{O_2} (feed/permeate)	References
Zirconia-based dual-phase membrane							
1	$\text{Zr}_{0.79}\text{Sc}_{0.2}\text{Ce}_{0.01}\text{O}_{2-\delta}-\text{La}_{0.7}\text{Sr}_{0.3}\text{MnO}_{3\pm\delta}$	$\text{Nd}_2\text{NiO}_{4+\delta}$	42.7	750 800 850 900	0.30 0.59 1.03 1.60	Air/He	[106]
2	$\text{Zr}_{0.79}\text{Sc}_{0.2}\text{Ce}_{0.01}\text{O}_{2-\delta}-\text{La}_{0.7}\text{Sr}_{0.3}\text{MnO}_{3\pm\delta}$	$\text{Nd}_2\text{NiO}_{4+\delta}$	40.8	800 850 900	0.59 1.03 1.65	Air/He	[8]
3	$(\text{ZrO}_2)_{0.92}(\text{Y}_2\text{O}_3)_{0.08}-\text{La}_{0.7}\text{Sr}_{0.3}\text{MnO}_{3\pm\delta}$	Pt	100	800 850 900 950	0.17 0.28 0.42 0.54	Air/He	[107]
4	$(\text{ZrO}_2)_{0.89}(\text{Y}_2\text{O}_3)_{0.01}(\text{Sc}_2\text{O}_3)_{0.10}-\text{LaCr}_{0.85}\text{Cu}_{0.10}\text{Ni}_{0.05}\text{O}_{3-\delta}$	$(\text{Y}_2\text{O}_3)_{0.08}(\text{ZrO}_2)_{0.92}-\text{(La}_{0.80}\text{Sr}_{0.20})\text{MnO}_{3-\delta}$	110	750 850 950 750 850 950	0.21 0.56 1.02 0.19 0.54 1.00	Air/ N_2 Air/ CO_2	[108]
Ceria-based dual-phase membrane							
5	$\text{Ce}_{0.9}\text{Gd}_{0.1}\text{O}_{2-\delta}-\text{La}_{0.7}\text{Ca}_{0.3}\text{Cr}_{0.95}\text{Zn}_{0.05}\text{O}_{3-\delta}$		800	875 900 950 975	0.02 0.03 0.06 0.08	Air/He	[109]
6	$\text{Ce}_{0.8}\text{Gd}_{0.2}\text{O}_{2-\delta}-\text{CoFe}_2\text{O}_4$		1000	850 900 950	0.10 0.14 0.19	Air/He	[110]
7	$\text{Ce}_{0.8}\text{Gd}_{0.2}\text{O}_{2-\delta}-\text{Cu}_{0.6}\text{Ni}_{0.4}\text{Mn}_2\text{O}_4$		800	700 800 900	0.03 0.07 0.14	Air/ N_2	[111]
8	$\text{Ce}_{0.8}\text{Sm}_{0.2}\text{O}_{2-\delta}-\text{PrBaCo}_2\text{O}_{5+\delta}$		600	850 900 925	0.20 0.27 0.32	Air/He	[112]
9	$\text{Ce}_{0.8}\text{Sm}_{0.05}\text{Bi}_{0.15}\text{O}_{2-\delta}-\text{Sm}_{0.6}\text{Sr}_{0.4}\text{Cu}_{0.2}\text{Fe}_{0.8}\text{O}_{3-\delta}$	$\text{Sm}_{0.5}\text{Sr}_{0.5}\text{CoO}_{3-\delta}$	500	800 850 900	0.37 0.62 0.83	Air/He	[113]
10	$\text{Ce}_{0.9}\text{Gd}_{0.1}\text{O}_{2-\delta}-\text{La}_{0.7}\text{Sr}_{0.3}\text{MnO}_3$	$\text{La}_{0.6}\text{Sr}_{0.4}\text{CoO}_{3-\delta}$	100	850	1.61	Air/He	[114]
11	$\text{Ce}_{0.9}\text{La}_{0.1}\text{O}_{2-\delta}-\text{La}_{0.6}\text{Sr}_{0.4}\text{Co}_{0.9}\text{Al}_{0.1}\text{O}_{3-\delta}$		600	1000 1000	1.02 0.72	Air/He Air/ CO_2	[115]
12	$\text{Ce}_{0.9}\text{Pr}_{0.1}\text{O}_{2-\delta}-\text{Pr}_{0.6}\text{Sr}_{0.4}\text{Fe}_{0.6}\text{Al}_{0.4}\text{O}_{3-\delta}$		400	900 950 1000	0.80 0.93 1.12	Air/He	[116]
13	$\text{Ce}_{0.9}\text{Pr}_{0.1}\text{O}_{2-\delta}-\text{Pr}_{0.6}\text{Sr}_{0.4}\text{Fe}_{0.99}\text{Bi}_{0.01}\text{O}_{3-\delta}$		600	800 850 900 950	0.09 0.15 0.26 0.48	Air/He	[117]

Table 1. Continued.

Nos.	Material	Active layer	Thickness [μm]	Temp. [°C]	Flux [mL cm ⁻² min ⁻¹]	P _{O₂} (feed/permeate)	References	
14	Ce _{0.85} Cd _{0.1} Cu _{0.05} O _{2-δ} -La _{0.6} Ca _{0.4} FeO _{3-δ}		500	1000	0.71	Air/CO ₂	[52]	
				850	0.05			
				900	0.09			
				950	0.25			
				1000	0.62			
				800	0.25	Air/He		
				850	0.40			
				900	0.61			
				950	0.87			
				800	0.15			
15	Ce _{0.85} Pr _{0.1} Cu _{0.05} O _{2-δ} -Pr _{0.4} Sr _{0.6} Fe _{0.95} Cu _{0.05} O _{3-δ}		600	850	0.28	Air/CO ₂	[118]	
				900	0.46			
				950	0.70			
				900	0.77			Air/He
				950	1.27			
				1000	1.60			
				900	0.41	Air/CO ₂		
				950	0.69			
				1000	0.98			
				850	0.11			
16	Ce _{0.8} Gd _{0.2} O _{2-δ} -FeCo ₂ O ₄	La _{0.6} Sr _{0.4} Co _{0.2} Fe _{0.8} O _{3-δ}	1000	850	0.11		Air/Ar	[76]
17	Ce _{0.8} Sm _{0.2} O _{2-δ} -PrBaCo ₂ O _{5+δ}	Ce _{0.8} Sm _{0.2} O _{2-δ} -PrBaCo ₂ O _{5+δ}	450	850	0.25	Air/He	[89]	
18	Ce _{0.9} Gd _{0.1} O _{2-δ} -La _{0.6} Sr _{0.4} Co _{0.2} Fe _{0.8} O _{3-δ}	La _{0.6} Sr _{0.4} CoO _{3-δ}	30	900	0.35	Air/He	[14]	
				945	0.48			
				800	2.78			
				850	3.63			
19	Ce _{0.9} Gd _{0.1} O _{2-δ} -La _{0.6} Sr _{0.4} Co _{0.2} Fe _{0.8} O _{3-δ}	La _{0.6} Sr _{0.4} CoO _{3-δ}	30	850	3.80	Air/He	[59]	
20	Ce _{0.9} Gd _{0.1} O _{2-δ} -La _{0.6} Sr _{0.4} Co _{0.2} Fe _{0.8} O _{3-δ}	SrCo _{0.1} Fe _{0.8} Nb _{0.1} O _{3-δ}	20	800	3.36	Air/He	[7]	
21	Ce _{0.9} Gd _{0.1} O _{2-δ} -La _{0.7} Sr _{0.3} MnO _{3±δ}			900	6.28	Air/CO ₂	[73]	
				1000	10.41			
				800	1.87			
				900	4.10			
				950	5.50			
				900	8.80			Air/He
				1000	14.0			
				850	1.50			
22	Ce _{0.9} Gd _{0.1} O _{2-δ} -La _{0.7} Sr _{0.3} MnO _{3±δ}	La _{0.6} Sr _{0.4} CoO _{3-δ}	30	750	1.17	Air/He	[15]	
23	Ce _{0.9} Gd _{0.1} O _{2-δ} -La _{0.7} Sr _{0.3} MnO _{3-δ}	Pr ₂ NiO _{4+δ}	25	800	1.66	Air/He	[104]	
				850	2.20			
				750	0.30			
				850	0.76			
				700	0.10			Air/CO ₂
775	0.32							
24	Ce _{0.9} Pr _{0.1} O _{2-δ} -Pr _{0.6} Ca _{0.4} FeO _{3-δ}	La _{0.6} Sr _{0.4} CoO _{3-δ}	300	900	0.58	Air/He	[69]	
				1000	1.00	Air/CO ₂		
				900	0.24			

Table 1. Continued.

Nos.	Material	Active layer	Thickness [μm]	Temp. [$^{\circ}\text{C}$]	Flux [$\text{mL cm}^{-2} \text{min}^{-1}$]	P_{O_2} (feed/permeate)	References
				1000	0.62		
25	$\text{Ce}_{0.8}\text{Sm}_{0.2}\text{O}_{1.9}\text{-SrCo}_{0.4}\text{Fe}_{0.55}\text{Zr}_{0.05}\text{O}_{3-\delta}$		600	950	2.69	5/0.005 atm	[119]
26	$\text{Ce}_{0.9}\text{Pr}_{0.1}\text{O}_{2-\delta}\text{-Pr}_{0.6}\text{Sr}_{0.4}\text{Fe}_{0.8}\text{Al}_{0.2}\text{O}_{3-\delta}$		330	900	0.59	Air/He	[120]
				950	0.78		
				1000	1.03		
27	$\text{Ce}_{0.9}\text{Pr}_{0.1}\text{O}_{2-\delta}\text{-Pr}_{0.6}\text{Sr}_{0.4}\text{Fe}_{0.99}\text{In}_{0.01}\text{O}_{3-\delta}$		600	800	0.19	Air/He	[121]
				900	0.48		
				1000	1.07		
				800	0.12	Air/ CO_2	
				900	0.22		
				1000	0.80		
28	$\text{Ce}_{0.8}\text{La}_{0.15}\text{Cu}_{0.05}\text{O}_{2-\delta}\text{-La}_{0.15}\text{Sr}_{0.85}\text{FeO}_{3-\delta}$		600	800	0.19	Air/He	[122]
				900	0.49		
				950	0.65		
29	$\text{Ce}_{0.85}\text{Sm}_{0.15}\text{O}_{1.925}\text{-Sm}_{0.6}\text{Sr}_{0.4}\text{Al}_{0.3}\text{Fe}_{0.7}\text{O}_{3-\delta}$	$\text{Sm}_{0.5}\text{Sr}_{0.5}\text{CoO}_{3-\delta}$	500	850	0.44	Air/He	[123]
				950	0.68		
				950	0.64	Air/ CO_2	
30	$\text{Ce}_{0.85}\text{Sm}_{0.15}\text{O}_{1.925}\text{-Sm}_{0.6}\text{Sr}_{0.4}\text{Cr}_{0.3}\text{Fe}_{0.7}\text{O}_{3-\delta}$	$\text{Sm}_{0.5}\text{Sr}_{0.5}\text{CoO}_{3-\delta}$	500	850	0.30	Air/He	[124]
				950	0.53		
		$\text{LiLaNiO}/\gamma\text{-Al}_2\text{O}_3$		850	3.99	Air/ CH_4	
				950	7.60		
31	$\text{Ce}_{0.9}\text{Pr}_{0.1}\text{O}_{2-\delta}\text{-Pr}_{0.6}\text{Ca}_{0.4}\text{FeO}_{3-\delta}$		600	1000	0.51	Air/He	[125]
				1000	0.25	Air/ CO_2	
32	$\text{Ce}_{0.9}\text{Pr}_{0.1}\text{O}_{2-\delta}\text{-Nd}_{0.5}\text{Sr}_{0.5}\text{Fe}_{0.9}\text{Cu}_{0.1}\text{O}_{3-\delta}$		650	750	0.23	Air/He	[126]
				850	0.46		
				950	1.02		
				950	0.63	Air/ CO_2	
33	$\text{Ce}_{0.8}\text{Gd}_{0.2}\text{O}_{2-\delta}\text{-Pr}_{0.6}\text{Sr}_{0.4}\text{Co}_{0.5}\text{Fe}_{0.4}\text{Nb}_{0.1}\text{O}_{3-\delta}$		500	850	0.27	Air/He	[127]
				900	0.45		
				925	0.54		
				850	0.16	Air/ CO_2	
				900	0.36		
				925	0.45		
34	$\text{Ce}_{0.8}\text{Sm}_{0.2}\text{O}_{1.9}\text{-Y}_{0.8}\text{Ca}_{0.2}\text{Cr}_{0.8}\text{Co}_{0.2}\text{O}_3$		1300	950	0.31	Air/ N_2	[128]
				950	2.89	Air/ CO_2 50% + (H_2 3% + N_2 97%) 50%	
				950	6.30	Air/ H_2 3% + N_2 97%	
35	$\text{Ce}_{0.8}\text{Gd}_{0.2}\text{O}_{2-\delta}\text{-Ba}_{0.95}\text{La}_{0.05}\text{Fe}_{0.975}\text{Nb}_{0.025}\text{O}_{3-\delta}$		1000	850	0.20	Air/He	[129]
				900	0.25		
				925	0.29		
				925	0.19	Air/ CO_2	
36	$\text{Ce}_{0.8}\text{Gd}_{0.2}\text{O}_{2-\delta}\text{-FeCo}_2\text{O}_4$	$\text{La}_{0.58}\text{Sr}_{0.4}\text{Co}_{0.2}\text{Fe}_{0.8}\text{O}_{3-\delta}$	1000	800	0.03	Air/Ar	[130]
				900	0.05		
				1015	0.08		
37	$\text{Ce}_{0.8}\text{Gd}_{0.2}\text{O}_{2-\delta}\text{-PrBaCo}_2\text{O}_{5+\delta}$		1000	800	0.17	Air/He	[131]

Table 1. Continued.

Nos.	Material	Active layer	Thickness [μm]	Temp. [$^{\circ}\text{C}$]	Flux [$\text{mL cm}^{-2} \text{min}^{-1}$]	P_{O_2} (feed/permeate)	References
38	$\text{Ce}_{0.8}\text{Gd}_{0.2}\text{O}_{2-\delta}$ -PrBaCo _{0.5} Fe _{1.5} O _{5+\delta}		600	850	0.25	Air/He	[132]
				900	0.32		
				925	0.38		
				800	0.28		
				850	0.39		
				900	0.51		
				925	0.56		
39	$\text{Ce}_{0.8}\text{Gd}_{0.15}\text{Cu}_{0.05}\text{O}_{2-\delta}$ -SrFeO _{3-δ}		500	925	0.36	Air/CO ₂ 50% + He 50%	[19]
				900	0.42	Air/He	
				900	0.63	O ₂ -enriched air (0.9 atm)/CO ₂	
40	$\text{Ce}_{0.8}\text{Nd}_{0.2}\text{O}_{2-\delta}$ -Nd _{0.5} Sr _{0.5} Al _{0.2} Fe _{0.8} O _{3-δ}		600	850	0.28	Air/He	[133]
				900	0.46		
				950	0.71		
				1000	0.99		
				850	0.09		
				900	0.24		
				950	0.51		
41	$\text{Ce}_{0.8}\text{Sm}_{0.2}\text{O}_{2-\delta}$ -Ba _{0.95} La _{0.05} Fe _{0.85} Zr _{0.15} O _{3-δ}		1000	1000	0.81	Air/CO ₂	[134]
				925	0.30		
				925	0.24		
				925	0.54		
				925	0.34		
42	$\text{Ce}_{0.8}\text{Sm}_{0.2}\text{O}_{1.9}$ -Sm _{0.8} Ca _{0.2} Mn _{0.5} Co _{0.5} O ₃	$\text{Ce}_{0.8}\text{Sm}_{0.2}\text{O}_{1.9}$ - SmMn _{0.5} Co _{0.5} O ₃	500	800	0.14	Air/He	[135]
				900	0.40		
				940	0.61		
				800	0.10		
				900	0.34		
				940	0.50		
				950	0.52		
43	$\text{Ce}_{0.8}\text{Sm}_{0.2}\text{O}_{2-\delta}$ -SrCo _{0.9} Nb _{0.1} O _{3-δ}		800	850	0.82	Air/He	[136]
				900	1.15		
				950	1.54		
				950	0.52		
				800	0.15		
				900	0.27		
				940	0.39		
44	$\text{Ce}_{0.9}\text{Gd}_{0.1}\text{O}_{1.95-\delta}$ -Al _{0.02} Ga _{0.02} Zn _{0.96} O _{1.02}	La _{0.6} Sr _{0.4} CoO _{3-δ}	1100	850	0.17	Air/CO ₂	[137]
				900	0.22		
				945	0.30		
				875	0.88		
				950	1.36		
				875	0.26		
				950	0.67		
45	$\text{Ce}_{0.9}\text{Gd}_{0.1}\text{O}_{2-\delta}$ -Ba _{0.5} Sr _{0.5} Co _{0.8} Fe _{0.2} O _{3-δ}		500	800	1.73	Air/He	[138]
				825	1.94		
46	$\text{Ce}_{0.9}\text{Gd}_{0.1}\text{O}_{2-\delta}$ -La _{0.6} Sr _{0.4} Co _{0.2} Fe _{0.8} O _{3-δ}	La _{0.6} Sr _{0.4} CoO _{3-δ}	60	800	1.73	Air/He	[139]
				825	1.94		

Table 1. Continued.

Nos.	Material	Active layer	Thickness [μm]	Temp. [$^{\circ}\text{C}$]	Flux [$\text{mL cm}^{-2} \text{min}^{-1}$]	P_{O_2} (feed/permeate)	References
47	$\text{Ce}_{0.9}\text{Gd}_{0.1}\text{O}_{2-\delta}\text{-SrCo}_{0.8}\text{Fe}_{0.1}\text{Nb}_{0.1}\text{O}_{3-\delta}$	$\text{Ce}_{0.9}\text{Gd}_{0.1}\text{O}_{2-\delta}\text{-SrCo}_{0.8}\text{Fe}_{0.1}\text{Nb}_{0.1}\text{O}_3$	1000	850	2.20	Air/He	[140]
				800	0.91		
				850	0.82		
48	$\text{Ce}_{0.9}\text{Nd}_{0.1}\text{O}_{2-\delta}\text{-Nd}_{0.6}\text{Sr}_{0.4}\text{CoO}_{3-\delta}$		400	900	0.74	Air/ CO_2	[141]
				900	0.50		
				900	0.56		
				950	0.76		
				1000	0.90		
49	$\text{Ce}_{0.9}\text{Nd}_{0.1}\text{O}_{2-\delta}\text{-Nd}_{0.6}\text{Sr}_{0.4}\text{FeO}_{3-\delta}$	$\text{La}_{0.6}\text{Sr}_{0.4}\text{CoO}_{3-\delta}$	600	950	0.55	Air/ CO_2	[18]
				850	0.19		
				900	0.29		
50	$\text{Ce}_{0.9}\text{Pr}_{0.1}\text{O}_{2-\delta}\text{-La}_{0.5}\text{Sr}_{0.5}\text{Fe}_{0.9}\text{Cu}_{0.1}\text{O}_{3-\delta}$		500	900	0.93	Air/He	[142]
				900	0.71		
				900	0.71		
51	$\text{Ce}_{0.9}\text{Pr}_{0.1}\text{O}_{2-\delta}\text{-Mn}_{1.5}\text{Co}_{1.5}\text{O}_{4-\delta}$		300	900	0.26	Air/ CO_2	[143]
				950	0.37		
				1000	0.48		
52	$\text{Ce}_{0.9}\text{Pr}_{0.1}\text{O}_{2-\delta}\text{-Pr}_{0.6}\text{Sr}_{0.4}\text{Fe}_{0.5}\text{Co}_{0.5}\text{O}_{3-\delta}$		600	800	0.24	Air/He	[144]
				900	0.59		
				1000	1.08		
				800	0.11		
				900	0.45		
53	$\text{Ce}_{0.9}\text{Gd}_{0.1}\text{O}_{2-\delta}\text{-Fe}_2\text{O}_3$		500	1000	1.01	Air/He	[67]
				900	0.06		
				950	0.10		
54	$\text{Ce}_{0.85}\text{Sm}_{0.15}\text{O}_{1.925}\text{-Sm}_{0.6}\text{Sr}_{0.4}\text{FeO}_{3-\delta}$	$\text{La}_{0.6}\text{Sr}_{0.4}\text{CoO}_{3-\delta}$	500	1000	0.18	Air/ CO_2	[68]
				1000	0.20		
				850	0.50		
55	$\text{Ce}_{0.8}\text{Sm}_{0.2}\text{O}_{2-\delta}\text{-Sm}_{0.3}\text{Sr}_{0.7}\text{Cu}_{0.2}\text{Fe}_{0.8}\text{O}_{3-\delta}$	Pd	1000	900	0.65	Air/He	[145]
				940	0.82		
				800	0.47		
				900	1.02		
				1000	2.05		
56	$\text{Ce}_{0.8}\text{Sm}_{0.2}\text{O}_{2-\delta}\text{-PrBaCo}_2\text{O}_{5+\delta}$	$\text{PrBaCo}_2\text{O}_{5+\delta}$	1000	800	0.43	Air/ CO_2	[32]
				900	0.93		
				1000	1.96		
57	$\text{Ce}_{0.8}\text{Sm}_{0.2}\text{O}_{1.9}\text{-Sm}_{0.6}\text{Ca}_{0.4}\text{CoO}_3$	$\text{Ce}_{0.8}\text{Sm}_{0.2}\text{O}_{1.9}\text{-Sm}_{0.6}\text{Ca}_{0.4}\text{CoO}_3$	500	850	0.28	Air/He	[146]
				900	0.40		
				940	0.51		
				850	0.11		
				900	0.14		
				950	0.18	Air/ CO_2	
				850	0.10		
				900	0.15		

Table 1. Continued.

Nos.	Material	Active layer	Thickness [μm]	Temp. [$^{\circ}\text{C}$]	Flux [$\text{mL cm}^{-2} \text{min}^{-1}$]	P_{O_2} (feed/permeate)	References
58	$\text{Ce}_{0.8}\text{Tb}_{0.2}\text{O}_{2-\delta}\text{--Fe}_2\text{NiO}_4$	Pr_6O_{11} -infiltrated $\text{Ce}_{0.8}\text{Tb}_{0.2}\text{O}_{2-\delta}\text{--Fe}_2\text{NiO}_4$	650	950	0.19	Air/Ar	[98]
				800	0.09		
				850	0.14		
				850	0.13		
59	$\text{Ce}_{0.9}\text{Gd}_{0.1}\text{O}_{2-\delta}\text{--NiFe}_2\text{O}_4$		500	900	0.11	Air/(CO ₂ 30% + Ar 70%)	[72]
				950	0.19	Air/He	
				1000	0.31	Air/CO ₂	
				900	0.09		
				950	0.16		
				1000	0.27		
60	$\text{Ce}_{0.8}\text{Sm}_{0.2}\text{O}_{2-\delta}\text{--La}_{0.7}\text{Ca}_{0.3}\text{CrO}_{3-\delta}$	$\text{Ce}_{0.8}\text{Sm}_{0.2}\text{O}_{2-\delta}\text{--Sm}_{0.5}\text{Sr}_{0.5}\text{Co}_{3-\delta}$	1000	850	0.05	Air/He	[147]
				900	0.09		
				950	0.14		
61	$\text{Ce}_{0.8}\text{Gd}_{0.2}\text{O}_{2-\delta}\text{--FeCo}_2\text{O}_4$	$\text{La}_{0.58}\text{Sr}_{0.4}\text{Co}_{0.2}\text{Fe}_{0.8}\text{O}_{3-\delta}$	950	910	0.03	Air/Ar	[77]
				960	0.05		
				1030	0.07		
62	$\text{Ce}_{0.8}\text{Tb}_{0.2}\text{O}_{2-\delta}\text{--NiFe}_2\text{O}_4$	$\text{Ce}_{0.8}\text{Gd}_{0.2}\text{O}_{2-\delta}\text{--La}_{0.8}\text{Sr}_{0.2}\text{MnO}_{3-\delta}$	770	900	0.11	Air/Ar	[82]
				950	0.17	Air/CO ₂	
				1000	0.25		
				900	0.15		
				950	0.22		
				1000	0.30		
63	$\text{Ce}_{0.8}\text{Tb}_{0.2}\text{O}_{2-\delta}\text{--NiFe}_2\text{O}_4$	Pd-infiltrated $\text{Ce}_{0.8}\text{Gd}_{0.2}\text{O}_{2-\delta}\text{--La}_{0.8}\text{Sr}_{0.2}\text{MnO}_{2-\delta}$	680	900	0.10	Air/Ar	[83]
				950	0.13		
				1000	0.17		
				900	0.09	Air/CO ₂	
				1000	0.20		

membrane.^[105] Kwon et al.^[8] demonstrated that the suppression of interfacial resistance between the active layer and zirconia-rich dual-phase membrane is a key factor in remarkably improved oxygen permeability (**Figure 11**). The ionic conduction, which is closely associated with the oxygen flux, is limited by secondary phases (e.g., SrZrO₃ and La₂Zr₂O₇) originating from the interdiffusion of zirconium with rare- and alkaline-earth metals such as strontium and lanthanum. By applying an active layer (NNO) having high surface exchange kinetics and low reactivity with zirconium, they improved the oxygen flux by orders of magnitude compared to that of membrane coated with representative perovskite active layers (e.g., LSC and LSCF). The strategy of using the membrane material as the active layer was also suggested to minimize the interfacial resistance of dual-phase membranes such as SDC-PBCO, SDC-Sm_{0.6}Ca_{0.4}O_{3- δ} ,

CTO-NFO, and SDC-SmMn_{0.5}Co_{0.5}O_{3- δ} . However, because of the low surface exchange coefficient of the CeO₂-based ionic conducting phase, the increase in oxygen permeability was smaller than that of the membrane to which a single-phase active layer such as LSC and LSCF was applied. A detailed list including the materials, performance, and experimental conditions of aforementioned dual-phase membranes is provided in **Table 1**. Many studies have been reported to improve the oxygen permeability and stability of the dual-phase membrane in terms of intrinsic and extrinsic properties. As mentioned in Section 2.2, the dual-phase membrane is composed of stabilized ZrO₂ and doped CeO₂ as an ionic conductor, and it can be seen that most research has been focused on CeO₂-based dual-phase membrane. This is due to the fact that CeO₂ has good chemical compatibility with the electronic conductor in the dual-phase

membrane compared with ZrO_2 , and thus shows high oxygen permeability. In order to improve the permeability, the thickness of the membrane should be as thin as possible, and as the thickness of the membrane becomes thinner, it is essential to understand not only bulk diffusion but also the surface exchange reaction. However, many studies focus on enhancing the oxygen permeability and stability by applying a new material or adjusting the doping level, as can be seen in Table 1.

4. Application Potential and Future Prospects of Dual-Phase Oxygen Transport Membranes

The oxygen transport membrane can afford process intensification via a coupling reaction on both sides of the membrane, suggesting that carbon neutrality can be approached by reducing carbon dioxide emissions and improving energy efficiency. Because fluorite-based dual-phase membranes, which were considered in this review, are chemically and mechanically stable, their potential for use as a catalytic membrane reactor to integrate separation and catalytic reaction has been demonstrated in many studies. Process intensification based on an oxygen transport membrane has been proposed, as shown in Figure 12. The coupling reaction can be achieved by splitting oxygen-containing gases (e.g., H_2O , NO , N_2O , and CO_2) in conjunction with other catalytic reactions such as the partial oxidation of methane (POM) and oxidative coupling of methane. Methane, which has abundant reserves, has received significant attention as an attractive reactant with high value-added potential because it can be converted into syngas (H_2 and CO) and ethylene

(C_2H_4), which are valuable in the petrochemical industry. Several studies have demonstrated that the integration of the two reactions in one membrane apparatus for process intensification is possible. Park et al.^[148] showed CO_2 utilization coupled with the POM through a chemically stable oxygen transport membrane ($\text{GDC-La}_{0.8}\text{Ca}_{0.2}\text{FeO}_{3-\delta}$) under pure CO_2 and CH_4 conditions. Jiang et al.^[149–151] reported a membrane reactor ($\text{BaCo}_x\text{Fe}_y\text{Zr}_{1-x-y}\text{O}_{3-\delta}$) capable of combining N_2O and NO removal with the simultaneous production of valuable chemicals from methane. Liang et al.^[152] experimentally demonstrated the generation of syngas on both sides of the membrane ($\text{Ce}_{0.8}\text{Pr}_{0.1}\text{O}_{2-\delta}-\text{Pr}_{0.6}\text{Sr}_{0.4}\text{FeO}_{3-\delta}$) by the simultaneous decomposition of water and carbon dioxide as well as the POM. Zhou et al.^[153] showed that water splitting and the coupling of methane to C_2 products were simultaneously performed by an $\text{SDC-Sr}_2\text{Fe}_{1.5}\text{Mo}_{0.5}\text{O}_{5+\delta}$ membrane reactor. The reported studies in coupling reactions using oxygen transport membrane are summarized in Table 2. Although oxygen transport membranes have advantages for use in catalytic membrane reactors to improve the efficiency of process intensification, membrane reactor technology is in its initial stages, and only a few studies have demonstrated its effectiveness in terms of performance and stability. Therefore, to develop high-performance membrane reactors toward energy-efficient and sustainable chemistry, it is important to find the optimal balance between performance and stability using various interdisciplinary approaches. Table 2 summarizes the reported studies in coupling reactions using oxygen transport membrane.

5. Conclusions

This review provides critical insight into intrinsic (internal aspect) and extrinsic properties (external aspect) improving the performance of the dual-phase membrane. The intrinsic factors that affect the performance enhancement of OTMs include the mechanical strength and oxygen ionic conductivity of the material constituting OTMs. As mentioned above, the single-phase membrane composed of perovskite structure with high oxygen permeability but low mechanical and chemical stabilities is difficult to apply for scale-up and modulation of OTMs. Thus, the mechanically and chemically stable dual-phase membrane with a fluorite structure (stabilized ZrO_2 , doped CeO_2) is a promising candidate for commercialization of OTMs. In the dual-phase membrane, the ionic conductivity of the fluorite structure, which is an oxygen ionic conductor, is an important factor in determining the oxygen permeability. However, in the case of stabilized ZrO_2 , it is easy to form secondary phases (e.g., $\text{La}_2\text{Zr}_2\text{O}_7$, SrZrO_3) by interdiffusion with a material applied as an electronic conductor of the dual-phase membrane. These secondary phases interfere with the transport of oxygen ions and result in lowering the overall ionic conductivity of the dual-phase membrane. Contrastively, doped CeO_2 has good chemical compatibility with electronic conductors compared with stabilized ZrO_2 , so the effect of lowering ionic conductivity due to secondary phase formation is insignificant. Thus, the higher oxygen permeability can be ensured when doped CeO_2 is used as an ionic conductor. To ensure oxygen transport in the membrane, electronic percolation is essential. However, because the ionic conductivity of

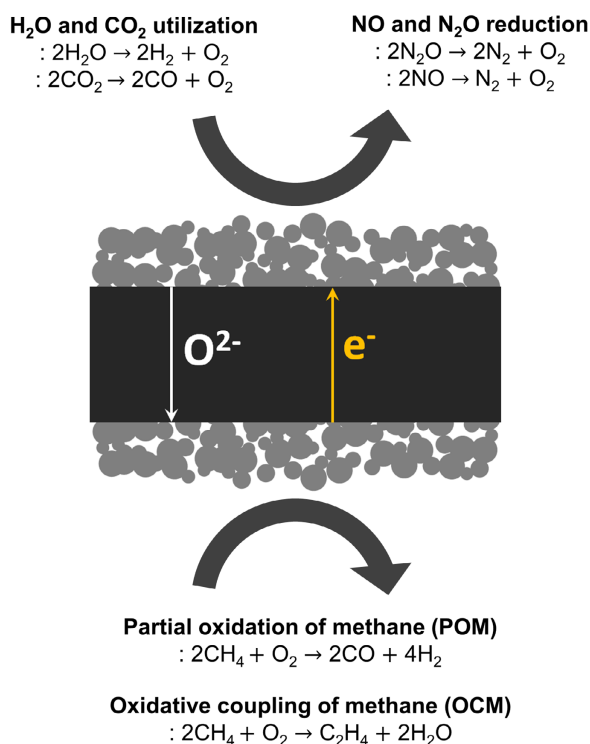


Figure 12. Schematic diagram of coupling reactions through fluorite-rich dual-phase oxygen transport membrane.

Table 2. Different oxygen transport membranes reported for the coupling reaction.

Nos.	Membrane	Catalyst	Temp. [°C]	O ₂ flux [mL cm ⁻² min ⁻¹]	Conversion	Selectivity	Yield	References
1	(La _{0.75} Sr _{0.25})(Cr _{0.5} Fe _{0.35} Ni _{0.15})O ₃	Fe–Ni alloy nanoparticles	900	–	CH ₄ 72% CO ₂ 81%	–	–	[154]
2	BaFe _{0.9} Zr _{0.05} Al _{0.05} O _{3-δ}		900	–	CH ₄ 97% N ₂ O 99.9%	CO 94%	91%	[155]
3	Nb ₂ O ₅ -doped SrCo _{0.8} Fe _{0.2} O _{3-δ}	Ni-based catalyst on Sr _{0.7} Ba _{0.3} Fe _{0.9} Mo _{0.1} O _{3-δ} Pd-based catalyst on (ZrO ₂) _{0.92} (Y ₂ O ₃) _{0.08} –La _{0.8} Sr _{0.2} MnO ₃	900	2.13	CH ₄ 84% CO ₂ 20.58%	CO 97%	81%	[156]
4	Ce _{0.8} Sm _{0.2} O _{1.9}	GdNi/Al ₂ O ₃ Pt	900	1.12	CH ₄ 37%	CO 86%	32%	[157]
5	Al ₂ O ₃ -doped SrCo _{0.8} Fe _{0.2} O _{3-δ}	Ni/Al ₂ O ₃	900	0.64	CH ₄ 86% CO ₂ 12.4%	CO 93%	80%	[158]
6	La _{0.8} Ca _{0.2} FeO _{3-δ} –Ce _{0.9} Gd _{0.1} O _{2-δ}	NiO–Ce _{0.9} Gd _{0.1} O _{2-δ} –La _{0.3} Sr _{0.7} TiO _{3-δ} La _{0.8} Ca _{0.2} FeO _{3-δ} –Ce _{0.9} Gd _{0.1} O _{2-δ}	900	2.3	CH ₄ 80% CO ₂ 40%	CO 100%	80%	[148]
7	Ba _{0.9} Co _{0.7} Fe _{0.2} Nb _{0.1} O _{3-δ}	Ni	875	16	CH ₄ 96.6%	CO 78.7%	76%	[159]
8	La _{0.8} Ca _{0.2} Fe _{0.94} O _{3-δ} –Ag	Ni/LaNiO ₃ /γ-Al ₂ O ₃	950	3.95	CH ₄ 58%	CO 89%	52%	[160]
9	La _{0.8} Ca _{0.2} Fe _{0.95} Ag _{0.05} O _{3-δ}	Ni/LaNiO ₃ /γ-Al ₂ O ₃	900	7.89	CH ₄ 99%	CO 93%	92%	[161]
10	BaBi _{0.05} Co _{0.8} Nb _{0.15} O _{3-δ}	Ni-phyllsilicate hollow sphere	750	–	CH ₄ 95% NO 100%	CO 94%	89%	[162]
11	Ce _{0.8} Sm _{0.2} O _{2-δ} –Sr ₂ Fe _{1.5} Mo _{0.5} O _{5+δ}	Ni/Al ₂ O ₃	950	0.75	CH ₄ 97%	CO 98%	95%	[163]
12	Zr _{0.92} Y _{0.08} O _{1.92} – La _{0.6} Sr _{0.4} Co _{0.2} Fe _{0.8} O _{3-δ}		900	–	CH ₄ 97.8%	CO 98.7%	97%	[5]
13	Ba _{0.5} Sr _{0.5} Co _{0.8} Fe _{0.2} O _{3-δ}	Ni/ZrO ₂	850	11	CH ₄ 98.8%	CO 91.5%	90%	[164]
14	BaCe _{0.1} Co _{0.4} Fe _{0.5} O _{3-δ}	LiLaNiO ₃ /γ-Al ₂ O ₃	950	9.5	CH ₄ 99%	CO 93%	92%	[165]
15	BaCo _{0.7} Fe _{0.2} Ta _{0.1} O _{3-δ}	Ni-based catalyst	900	16.2	CH ₄ 99%	CO 94%	93%	[166]
16	La _{0.6} Sr _{0.4} Ti _{0.3} Fe _{0.7} O ₃	NiO, La _{0.6} Sr _{0.4} CoO ₃	1000	11.3	CH ₄ 42.5%	CO 99%	42%	[167]
17	BaCo _{0.7} Fe _{0.2} Nb _{0.1} O _{3-δ}	Ni/Ce _{0.75} Zr _{0.25} O ₂ /Mg ₃ (Al)O Ce _{0.8} Re _{0.2} O _{2-δ}	875	19.8	CH ₄ 99.4%	CO 91.4%	91%	[168]
18	SrCoFeO _x	Ni/γ-Al ₂ O ₃	900	2.4	CH ₄ 88%	CO 97%	85%	[169]
19	BaCo _{0.7} Fe _{0.2} Nb _{0.1} O _{3-δ}	Ni-based catalyst	875	15	CH ₄ 92%	CO 104%	96%	[170]
20	BaCo _x Fe _y Zr _{1-x-y} O _{3-δ}	Ni/Al ₂ O ₃	850	–	C ₂ H ₆ 85% N ₂ O 100%	C ₂ H ₄ 86%	73%	[150]
21	BaCo _x Fe _y Zr _{1-x-y} O _{3-δ}		800	–	C ₂ H ₆ 59%	C ₂ H ₄ 89%	55%	[171]
22	La _{0.3} Sr _{0.7} Fe _{0.7} Cu _{0.2} Mo _{0.1} O ₃	La _{0.3} Sr _{0.7} Fe _{0.7} Cu _{0.2} Mo _{0.1} O ₃	900	7.9	CH ₄ 53% C ₂ H ₆ 11.8%	C ₂ H ₄ 24.7% 6%	13%	[172]
23	Ba _{0.5} Sr _{0.5} Co _{0.8} Fe _{0.2} O _{3-δ}	Mn–Na ₂ WO ₄ /SiO ₂	950	–	CH ₄ 26%	C ₂ 36%	6.5%	[173]
24	Ba _{0.5} Sr _{0.5} Co _{0.8} Fe _{0.2} O _{3-δ}	Mn–Na ₂ WO ₄ /SiO ₂	900	–	CH ₄ 54%	C ₂ 29%	15.6%	[174]
25	Ba _{0.5} Ce _{0.4} Gd _{0.1} Co _{0.8} Fe _{0.2} O _{3-δ}	Na–W–Mn/SiO ₂	850	1.4	CH ₄ 51.6%	C ₂ 67.4%	34.7%	[175]
26	BaCo _x Fe _y Zr _{1-x-y} O _{3-δ}	Mn–Na ₂ WO ₄ /SiO ₂	800	–	CH ₄ 34%	C ₂ 50%	17%	[176]

dual-phase membranes decreases with increasing electronic conductor content, it is necessary to minimize the electronic conductor content while maintaining percolation. When a pure electronic conductor is used as the electron path, it can adversely affect the oxygen permeability because it interferes with the diffusion of oxygen ions through the bulk membrane. By contrast, when an MIEC is applied as the electronic conductor, the ionic conductivity of the MIEC can provide an additional oxygen ion

path in the dual-phase membrane, improving the overall oxygen permeability. However, because MIEC materials generally have a high TEC, the mechanical and thermomechanical stability can be decreased by a TEC mismatch with the ionic conductor at elevated temperatures.

On the other hand, the external factors include concentration polarization and thickness of the membrane. There are a lot of different mechanisms involved in oxygen permeation, which can

be understood as a series of resistances. If feed and permeate sides are not sufficiently supplied with sweep gas, or if the porosity of the active coating layer at both sides of the membrane is not sufficient, this can generate a lower oxygen concentration gradient, resulting in a decrease in the oxygen chemical potential; this phenomenon is termed as a concentration polarization, which can significantly reduce oxygen permeation performance. Thus, in order to obtain optimized oxygen permeation flux by excluding the influence of the concentration polarization, a sufficient amount of sweep gas must be supplied to the feed and permeate sides, and the porosity of the active layer should also be sufficient to facilitate gas diffusion. Thickness of membrane can also play an important role in improving oxygen permeation flux, and it can be confirmed that oxygen permeation flux increases with decreasing membrane thickness according to Wagner equation. However, as the membrane becomes thinner, surface exchange becomes the rate-determining step in oxygen permeation, where the oxygen flux is limited by both bulk diffusion and surface exchange. Thus, in order to improve the oxygen permeation flux, it is essential not only to lower the thickness of the membrane, but also to apply an active coating layer to promote the surface exchange kinetics. In summary, it can be concluded that the study of the surface exchange reaction plays an important role in improving the oxygen permeability of the dual-phase membrane.

Although numerous studies on oxygen transport membranes have been conducted in recent years, the trade-off relationship between oxygen permeability and stability is still considered a decisive problem to be solved for the commercialization of oxygen transport membranes. Thus, further investigation of dual-phase membranes is urgently needed to ensure sufficient oxygen permeability and stability for commercialization.

Acknowledgements

Y.K. and G.D.N. contributed equally to this work. This work was supported by the National Research Foundation of Korea (NRF) grant funded by the Korean government (Ministry of Science and ICT [MSIT]) (NRF-2022R1A2B5B02001873). This research was also supported by the program of Future Hydrogen Original Technology Development (NRF-2021M3I3A1084929), through the National Research Foundation of Korea (NRF), funded by the Korean government (MSIT).

Conflict of Interest

The authors declare no conflict of interest.

Keywords

active coating layers, bulk diffusions, dual-phase composites, oxygen surface exchanges, oxygen transport membranes

Received: May 30, 2022

Revised: July 31, 2022

Published online: September 11, 2022

[1] T. Burdyny, H. Struchtrup, *Energy* **2010**, 35, 1884.

[2] S. P. Badwal, F. T. Ciacchi, *Adv. Mater.* **2001**, 13, 993.

- [3] X. Zhu, W. Yang, *Adv. Mater.* **2019**, 31, 1902547.
- [4] Z. Li, Y. Deng, N. Dewangan, J. Hu, Z. Wang, X. Tan, S. Liu, S. Kawi, *Chem. Eng. J.* **2021**, 420, 129834.
- [5] J. Shi, X. Zhu, K. Li, Y. Wei, H. Wang, *Fuel Cells* **2021**, 21, 58.
- [6] X. Xia, H. Zhou, Y. Zhang, H. Jiang, *AIChE J.* **2019**, 65, e16740.
- [7] G. D. Nam, G. Lee, S. Choi, J. Lee, S.-J. Song, J. H. Joo, *J. Mater. Chem. A* **2020**, 8, 23884.
- [8] Y.-I. Kwon, J. H. Park, S. M. Kang, G. D. Nam, J. W. Lee, J. H. Kim, D. Kim, S. M. Jeong, J. H. Yu, J. H. Joo, *Energy Environ. Sci.* **2019**, 12, 1358.
- [9] R. Kiebach, S. Pirou, L. M. Aguilera, A. B. Haugen, A. Kaiser, P. V. Hendriksen, M. Balaguer, J. García-Fayos, J. M. Serra, F. Schulze-Küppers, *J. Mater. Chem. A* **2022**, 10, 2152.
- [10] J. Sunarso, S. Baumann, J. Serra, W. Meulenber, S. Liu, Y. Lin, J. D. Da Costa, *J. Membr. Sci.* **2008**, 320, 13.
- [11] G. Chen, A. Feldhoff, A. Weidenkaff, C. Li, S. Liu, X. Zhu, J. Sunarso, K. Huang, X. Y. Wu, A. F. Ghoniem, *Adv. Funct. Mater.* **2022**, 32, 2105702.
- [12] C. Li, J. J. Chew, A. Mahmoud, S. Liu, J. Sunarso, *J. Membr. Sci.* **2018**, 567, 228.
- [13] F. Schulze-Küppers, S. Baumann, W. Meulenber, H. Bouwmeester, *J. Membr. Sci.* **2020**, 596, 117704.
- [14] J. H. Joo, K. S. Yun, Y. Lee, J. Jung, C.-Y. Yoo, J. H. Yu, *Chem. Mater.* **2014**, 26, 4387.
- [15] J. H. Joo, K. S. Yun, J.-H. Kim, Y. Lee, C.-Y. Yoo, J. H. Yu, *ACS Appl. Mater. Interfaces* **2015**, 7, 14699.
- [16] S. Baumann, J. Serra, M. Lobera, S. Escolástico, F. Schulze-Küppers, W. Meulenber, *J. Membr. Sci.* **2011**, 377, 198.
- [17] C. Yacou, J. Sunarso, C. X. Lin, S. Smart, S. Liu, J. C. D. da Costa, *J. Membr. Sci.* **2011**, 380, 223.
- [18] H. Luo, T. Klande, Z. Cao, F. Liang, H. Wang, J. Caro, *J. Mater. Chem. A* **2014**, 2, 7780.
- [19] W. Fang, F. Steinbach, C. Chen, A. Feldhoff, *Chem. Mater.* **2015**, 27, 7820.
- [20] M. Arnold, H. Wang, A. Feldhoff, *J. Membr. Sci.* **2007**, 293, 44.
- [21] A. Waindich, A. Möbius, M. Müller, *J. Membr. Sci.* **2009**, 337, 182.
- [22] Q. Zhu, T. Jin, Y. Wang, *Solid State Ionics* **2006**, 177, 1199.
- [23] H. Luo, H. Jiang, T. Klande, Z. Cao, F. Liang, H. Wang, J. Caro, *Chem. Mater.* **2012**, 24, 2148.
- [24] P. Manning, J. Sirman, J. Kilner, *Solid State Ionics* **1996**, 93, 125.
- [25] A. Berenov, A. Atkinson, J. Kilner, E. Bucher, W. Sitte, *Solid State Ionics* **2010**, 181, 819.
- [26] Y. Lin, *Sep. Purif. Technol.* **2001**, 25, 39.
- [27] P. Niehoff, S. Baumann, F. Schulze-Küppers, R. Bradley, I. Shapiro, W. Meulenber, P. Withers, R. Vaßen, *Sep. Purif. Technol.* **2014**, 121, 60.
- [28] H. Bouwmeester, H. Kruidhof, A. Burggraaf, *Solid State Ionics* **1994**, 72, 185.
- [29] H. Bouwmeester, P. J. Gellings, *The CRC Handbook of Solid State Electrochemistry*, CRC Press, Enschede **1997**.
- [30] B. Kakati, D. Sathiyamoorthy, A. Verma, *Int. J. Hydrogen Energy* **2011**, 36, 14851.
- [31] R. A. Cutler, D. L. Meixner, *Solid State Ionics* **2003**, 159, 9.
- [32] T. Chen, H. Zhao, Z. Xie, J. Wang, Y. Lu, N. Xu, *J. Power Sources* **2013**, 223, 289.
- [33] F. Zeng, J. Malzbender, S. Baumann, M. Krüger, L. Winnubst, O. Guillon, W. A. Meulenber, *J. Eur. Ceram. Soc.* **2020**, 40, 5646.
- [34] V. Gorelov, *Solid State Phys.* **2019**, 61, 1288.
- [35] G. K. Sidhu, R. Kumar, *Appl. Surf. Sci.* **2017**, 392, 598.
- [36] F. del Monte, W. Larsen, J. D. Mackenzie, *J. Am. Ceram. Soc.* **2000**, 83, 628.
- [37] S. Yoon, T. Noh, W. Kim, J. Choi, H. Lee, *Ceram. Int.* **2013**, 39, 9247.
- [38] S. Badwal, *Solid State Ionics* **1992**, 52, 23.
- [39] F. Ciacchi, S. Badwal, *J. Eur. Ceram. Soc.* **1991**, 7, 197.

- [40] J. Kimpton, T. Randle, J. Drennan, *Solid State Ionics* **2002**, 149, 89.
- [41] F. Yuan, J. Wang, H. Miao, C. Guo, W. G. Wang, *J. Alloys Compd.* **2013**, 549, 200.
- [42] C. Haering, A. Roosen, H. Schichl, M. Schnöller, *Solid State Ionics* **2005**, 176, 261.
- [43] C. S. Suci, E. S. Erichsen, A. C. Hoffmann, E. Dorolti, R. Tetea, *ECS Trans.* **2009**, 25, 1679.
- [44] O. Yamamoto, Y. Arati, Y. Takeda, N. Imanishi, Y. Mizutani, M. Kawai, Y. Nakamura, *Solid State Ionics* **1995**, 79, 137.
- [45] X. Chen, K. Khor, S. Chan, L. Yu, *Mater. Sci. Eng., A* **2002**, 335, 246.
- [46] H. Inaba, H. Tagawa, *Solid State Ionics* **1996**, 83, 1.
- [47] B. C. Steele, *Solid State Ionics* **2000**, 129, 95.
- [48] S. Wang, T. Kobayashi, M. Dokiya, T. Hashimoto, *J. Electrochem. Soc.* **2000**, 147, 3606.
- [49] C. Chen, H. Kruidhof, H. Bouwmeester, H. Verweij, A. Burggraaf, *Solid State Ionics* **1996**, 86, 569.
- [50] T. H. Lee, Y. L. Yang, A. J. Jacobson, *Solid State Ionics* **2000**, 134, 331.
- [51] P. Seeharaj, A. Atkinson, *Solid State Ionics* **2011**, 204, 46.
- [52] W. Fang, F. Liang, Z. Cao, F. Steinbach, A. Feldhoff, *Angew. Chem., Int. Ed.* **2015**, 54, 4847.
- [53] H. Ullmann, N. Trofimenko, F. Tietz, D. Stöver, A. Ahmad-Khanlou, *Solid State Ionics* **2000**, 138, 79.
- [54] T. Hong, L. Zhang, F. Chen, C. Xia, *J. Power Sources* **2012**, 218, 254.
- [55] A. Esquirol, J. Kilner, N. Brandon, *Solid State Ionics* **2004**, 175, 63.
- [56] J. Lane, J. Kilner, *Solid State Ionics* **2000**, 136, 927.
- [57] P. Seeharaj, A. Berenov, E. Raj, R. Rudkin, A. Atkinson, *Solid State Ionics* **2011**, 192, 638.
- [58] S. B. Adler, J. Lane, B. Steele, *J. Electrochem. Soc.* **1996**, 143, 3554.
- [59] Y.-I. Kwon, B. T. Na, J. H. Park, K. S. Yun, S. K. Hong, J. H. Yu, J. H. Joo, *J. Membr. Sci.* **2017**, 535, 200.
- [60] X. Xu, Y. Zhong, Z. Shao, *Trends Chem.* **2019**, 1, 410.
- [61] A. Petrov, O. Kononchuk, A. Andreev, V. Cherepanov, P. Kofstad, *Solid State Ionics* **1995**, 80, 189.
- [62] A. Egger, E. Bucher, M. Yang, W. Sitte, *Solid State Ionics* **2012**, 225, 55.
- [63] M. Matsuda, K. Ihara, M. Miyake, *Solid State Ionics* **2004**, 172, 57.
- [64] M. Mogensen, T. Lindgaard, U. R. Hansen, G. Mogensen, *J. Electrochem. Soc.* **1994**, 141, 2122.
- [65] J. Hwang, H. Lee, K. J. Yoon, H.-W. Lee, B.-K. Kim, J.-H. Lee, J.-W. Son, *J. Electrochem. Soc.* **2012**, 159, F639.
- [66] H. J. Park, S. Kim, *Electrochem. Solid-State Lett.* **2007**, 10, B187.
- [67] H. Luo, H. Jiang, K. Efimov, F. Liang, H. Wang, J. Caro, *Ind. Eng. Chem. Res.* **2011**, 50, 13508.
- [68] X. Zhu, M. Li, H. Liu, T. Zhang, Y. Cong, W. Yang, *J. Membr. Sci.* **2012**, 394, 120.
- [69] S. Wang, L. Shi, Z. Xie, Y. He, D. Yan, M.-R. Li, J. Caro, H. Luo, *J. Eur. Ceram. Soc.* **2019**, 39, 4882.
- [70] H. Huang, S. Cheng, J. Gao, C. Chen, J. Yi, *Mater. Lett.* **2014**, 137, 245.
- [71] S. K. Kim, M. J. Shin, J. Rufner, K. van Benthem, J. H. Yu, S. Kim, *J. Membr. Sci.* **2014**, 462, 153.
- [72] H. Luo, K. Efimov, H. Jiang, A. Feldhoff, H. Wang, J. Caro, *Angew. Chem., Int. Ed.* **2011**, 50, 759.
- [73] B. T. Na, J. H. Park, J. H. Park, J. H. Yu, J. H. Joo, *ACS Appl. Mater. Interfaces* **2017**, 9, 19917.
- [74] L.-W. Tai, M. Nasrallah, H. Anderson, D. Sparlin, S. Sehlin, *Solid State Ionics* **1995**, 76, 259.
- [75] L.-W. Tai, M. Nasrallah, H. Anderson, D. Sparlin, S. Sehlin, *Solid State Ionics* **1995**, 76, 273.
- [76] M. Ramasamy, S. Baumann, J. Palisaitis, F. Schulze-Küppers, M. Balaguer, D. Kim, W. A. Meulenberg, J. Mayer, R. Bhawe, O. Guillon, *J. Am. Ceram. Soc.* **2016**, 99, 349.
- [77] F. Zeng, S. Baumann, J. Malzbender, A. Nijmeijer, L. Winnubst, O. Guillon, R. Schwaiger, W. A. Meulenberg, *J. Membr. Sci.* **2021**, 628, 119248.
- [78] C. Gaudillere, J. Garcia-Fayos, M. Balaguer, J. M. Serra, *ChemSusChem* **2014**, 7, 2554.
- [79] R. Wandekar, B. Wani, S. Bharadwaj, *Mater. Lett.* **2005**, 59, 2799.
- [80] S. Jiang, W. Wang, *Solid State Ionics* **2005**, 176, 1351.
- [81] J. Garcia-Fayos, M. Balaguer, S. Baumann, J. M. Serra, *J. Membr. Sci.* **2018**, 548, 117.
- [82] J. Garcia-Fayos, M. Balaguer, J. M. Serra, *ChemSusChem* **2015**, 8, 4242.
- [83] M. Balaguer, J. Garcia-Fayos, C. Solís, J. M. Serra, *Chem. Mater.* **2013**, 25, 4986.
- [84] R. De Souza, J. Kilner, *Solid State Ionics* **1998**, 106, 175.
- [85] A. Chang, S. J. Skinner, J. A. Kilner, *Solid State Ionics* **2006**, 177, 2009.
- [86] H. Jung, Y. Kim, P. Connor, J. Irvine, J. Bae, W. Zhou, *J. Power Sources* **2009**, 194, 704.
- [87] A. Taskin, A. Lavrov, Y. Ando, *Appl. Phys. Lett.* **2005**, 86, 091910.
- [88] G. Kim, S. Wang, A. Jacobson, L. Reimus, P. Brodersen, C. Mims, *J. Mater. Chem.* **2007**, 17, 2500.
- [89] T. Chen, H. Zhao, Z. Xie, Y. Lu, N. Xu, *Int. J. Hydrogen Energy* **2012**, 37, 19133.
- [90] Z. Zhao, L. Liu, X. Zhang, W. Wu, B. Tu, D. Cui, D. Ou, M. Cheng, *Int. J. Hydrogen Energy* **2013**, 38, 15361.
- [91] A. Basile, S. P. Nunees, *Advanced Membrane Science and Technology for Sustainable Energy and Environmental Applications*, Woodhead Publishing, Cambridge, UK **2011**.
- [92] I. Thaheem, K. J. Kim, J. J. Lee, D. W. Joh, I. Jeong, K. T. Lee, *J. Mater. Chem. A* **2019**, 7, 19696.
- [93] P. Li, N. Duan, J. Ma, L. Jia, B. Chi, J. Pu, J. Li, J.-L. Luo, *Int. J. Hydrogen Energy* **2019**, 44, 31333.
- [94] Y. Rao, Z. Wang, L. Chen, R. Wu, R. Peng, Y. Lu, *Int. J. Hydrogen Energy* **2013**, 38, 14329.
- [95] Q. Zhao, Z. Yan, C. Chen, J. Chen, *Chem. Rev.* **2017**, 117, 10121.
- [96] R. W. Grimes, A. B. Anderson, A. H. Heuer, *J. Am. Chem. Soc.* **1989**, 111, 1.
- [97] A. Seko, K. Yuge, F. Oba, A. Kuwabara, I. Tanaka, *Phys. Rev. B: Condens. Matter* **2006**, 73, 184117.
- [98] J. Garcia-Fayos, R. Ruhl, L. Navarrete, H. J. Bouwmeester, J. M. Serra, *J. Mater. Chem. A* **2018**, 6, 1201.
- [99] D. Lee, H. N. Lee, *Materials* **2017**, 10, 368.
- [100] S. Park, Y. Kim, Y. Noh, T. Kim, H. Han, W. Yoon, J. Choi, S.-H. Yi, W.-J. Lee, W. B. Kim, *J. Mater. Chem. A* **2020**, 8, 138.
- [101] X. Xu, Y. Pan, Y. Zhong, R. Ran, Z. Shao, *Mater. Horiz.* **2020**, 7, 2519.
- [102] P. Kaur, K. Singh, *Ceram. Int.* **2020**, 46, 5521.
- [103] K. Padmasree, K.-Y. Lai, W. Kaveevivitchai, A. Manthiram, *J. Power Sources* **2018**, 374, 249.
- [104] K. S. Yun, J. H. Park, Y.-I. Kwon, D. Y. Kim, C.-Y. Yoo, J. H. Yu, J. H. Joo, *J. Mater. Chem. A* **2016**, 4, 13549.
- [105] S. Lee, K. S. Lee, S. K. Woo, J. W. Kim, T. Ishihara, D. K. Kim, *Solid State Ionics* **2003**, 158, 287.
- [106] J. H. Park, S. M. Kang, Y.-I. Kwon, G. D. Nam, K. S. Yun, S.-J. Song, J. H. Yu, J. H. Joo, *J. Membr. Sci.* **2020**, 597, 117620.
- [107] K. S. Yun, C.-Y. Yoo, S.-G. Yoon, J. H. Yu, J. H. Joo, *J. Membr. Sci.* **2015**, 486, 222.
- [108] S. Pirou, J. M. Bermudez, B. T. Na, S. Ovtar, J. H. Yu, P. V. Hendriksen, A. Kaiser, T. R. Reina, M. Millan, R. Kiebach, *J. Membr. Sci.* **2018**, 552, 115.
- [109] T. Zhu, Z. Yang, M. Han, *J. Mater. Sci. Technol.* **2014**, 30, 954.
- [110] Y. Lin, S. Fang, D. Su, K. S. Brinkman, F. Chen, *Nat. Commun.* **2015**, 6, 6824.
- [111] U. Pippardt, J. Böer, C. Bollert, A. Hoffmann, M. Heidenreich, R. Krieger, M. Schulz, A. Simon, *J. Ceram. Sci. Technol.* **2014**, 5, 309.
- [112] T. Chen, H. Zhao, Z. Xie, L. Feng, X. Lu, W. Ding, F. Li, *Int. J. Hydrogen Energy* **2012**, 37, 5277.

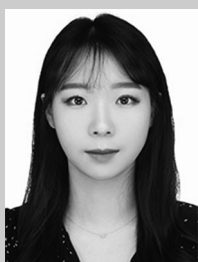
- [113] S. Huang, W. Li, Z. Cao, H. Li, H. Ma, X. Zhu, W. Yang, *J. Membr. Sci.* **2019**, 579, 342.
- [114] J. H. Joo, K. S. Yun, C.-Y. Yoo, J. H. Yu, *J. Mater. Chem. A* **2014**, 2, 8174.
- [115] D. Li, X. Wang, W. Tan, Y. Huang, L. Zeng, Y. He, P. Yu, H. Luo, *Sep. Purif. Technol.* **2021**, 274, 119042.
- [116] L. Shi, S. Wang, T. Lu, Y. He, D. Yan, Q. Lan, Z. Xie, H. Wang, M. Boubeche, H. Luo, *Ceram. Int.* **2019**, 45, 20033.
- [117] C. Zhang, Y. Huang, L. Zeng, Y. He, P. Yu, H. Luo, *Processes* **2021**, 9, 1767.
- [118] X. Wang, Y. Huang, D. Li, L. Zeng, Y. He, M. Boubeche, H. Luo, *J. Membr. Sci.* **2021**, 633, 119403.
- [119] J. Chua, C. Li, J. Sunarso, *IOP Conf. Ser.: Mater. Sci. Eng.* **2021**, 1195, 012060.
- [120] L. Shi, S. Wang, T. Lu, Y. He, D. Yan, Q. Lan, Z. Xie, H. Wang, M.-R. Li, J. Caro, *J. Alloys Compd.* **2019**, 806, 500.
- [121] Y. Huang, C. Zhang, X. Wang, D. Li, L. Zeng, Y. He, P. Yu, H. Luo, *Ceram. Int.* **2022**, 48, 415.
- [122] Z. Du, Y. Ma, H. Zhao, K. Li, Y. Lu, *J. Membr. Sci.* **2019**, 574, 243.
- [123] X. Zhu, Y. Liu, Y. Cong, W. Yang, *Solid State Ionics* **2013**, 253, 57.
- [124] L. Cai, W. Li, Z. Cao, X. Zhu, W. Yang, *J. Membr. Sci.* **2016**, 520, 607.
- [125] S. Wang, L. Shi, M. Boubeche, X. Wang, L. Zeng, H. Wang, Z. Xie, W. Tan, H. Luo, *Sep. Purif. Technol.* **2020**, 251, 117361.
- [126] G. Chen, Z. Zhao, M. Widenmeyer, R. Yan, L. Wang, A. Feldhoff, A. Weidenkaff, *Membranes* **2020**, 10, 183.
- [127] H. Cheng, P. Wang, H. Zhao, K. Li, X. Lu, Q. Xu, *Ceram. Int.* **2017**, 43, 6477.
- [128] K. J. Yoon, O. A. Marina, *J. Membr. Sci.* **2016**, 499, 301.
- [129] H. Cheng, N. Zhang, X. Xiong, X. Lu, H. Zhao, S. Li, Z. Zhou, *ACS Sustainable Chem. Eng.* **2015**, 3, 1982.
- [130] M. Ramasamy, E. Persoon, S. Baumann, M. Schroeder, F. Schulze-Küppers, D. Görtz, R. Bhave, M. Bram, W. Meulenber, *J. Membr. Sci.* **2017**, 544, 278.
- [131] L. Luo, H. Cheng, G. Li, X. Lu, B. Jiang, *J. Energy Chem.* **2015**, 24, 15.
- [132] B. Jiang, H. Cheng, L. Luo, X. Lu, Z. Zhou, *J. Mater. Sci. Technol.* **2014**, 30, 1174.
- [133] K. Partovi, M. Bittner, J. Caro, *J. Mater. Chem. A* **2015**, 3, 24008.
- [134] H. Cheng, L. Luo, W. Yao, X. Lu, X. Zou, Z. Zhou, *J. Membr. Sci.* **2015**, 492, 220.
- [135] X. Zhu, H. Liu, Y. Cong, W. Yang, *Chem. Commun.* **2012**, 48, 251.
- [136] S. Guo, Z. Liu, J. Zhu, X. Jiang, Z. Song, W. Jin, *Fuel Process. Technol.* **2016**, 154, 19.
- [137] S. Cheng, M. Søgaard, L. Han, W. Zhang, M. Chen, A. Kaiser, P. V. Hendriksen, *Chem. Commun.* **2015**, 51, 7140.
- [138] J. Xue, Q. Liao, Y. Wei, Z. Li, H. Wang, *J. Membr. Sci.* **2013**, 443, 124.
- [139] K. Raju, S. Kim, E. J. Kang, K. S. Yun, Y.-H. Seong, I.-S. Han, H.-K. Lee, J. H. Yu, *J. Eur. Ceram. Soc.* **2021**, 41, 4884.
- [140] J. Zhou, X. Tang, D. He, C. Wu, Y. Zhang, W. Ding, Y. Jin, C. Sun, *J. Alloys Compd.* **2015**, 646, 204.
- [141] Y. He, L. Shi, F. Wu, W. Xie, S. Wang, D. Yan, P. Liu, M.-R. Li, J. Caro, H. Luo, *J. Mater. Chem. A* **2018**, 6, 84.
- [142] G. Chen, B. Tang, M. Widenmeyer, L. Wang, A. Feldhoff, A. Weidenkaff, *J. Membr. Sci.* **2020**, 595, 117530.
- [143] H. Luo, H. Jiang, T. Klande, F. Liang, Z. Cao, H. Wang, J. Caro, *J. Membr. Sci.* **2012**, 423, 450.
- [144] F. Liang, H. Luo, K. Partovi, O. Ravkina, Z. Cao, Y. Liu, J. Caro, *Chem. Commun.* **2014**, 50, 2451.
- [145] E. Magnone, J. Chae, J. H. Park, *Ceram. Int.* **2018**, 44, 12948.
- [146] H. Li, Y. Liu, X. Zhu, Y. Cong, S. Xu, W. Xu, W. Yang, *Sep. Purif. Technol.* **2013**, 114, 31.
- [147] S. Fang, C. Chen, L. Winnubst, *Solid State Ionics* **2011**, 190, 46.
- [148] J. H. Park, Y.-I. Kwon, G. D. Nam, J. H. Joo, *J. Mater. Chem. A* **2018**, 6, 14246.
- [149] H. Jiang, H. Wang, F. Liang, S. Werth, T. Schiestel, J. Caro, *Angew. Chem., Int. Ed.* **2009**, 48, 2983.
- [150] H. Jiang, H. Wang, F. Liang, S. Werth, S. Schirrmeister, T. Schiestel, J. Caro, *Catal. Today* **2010**, 156, 187.
- [151] H. Jiang, L. Xing, O. Czuprat, H. Wang, S. Schirrmeister, T. Schiestel, J. Caro, *Chem. Commun.* **2009**, 44, 6738.
- [152] W. Liang, Z. Cao, G. He, J. Caro, H. Jiang, *ACS Sustainable Chem. Eng.* **2017**, 5, 8657.
- [153] H. Zhou, W. Liang, F. Liang, H. Jiang, *Catal. Today* **2019**, 331, 2.
- [154] D. Papargyriou, D. N. Miller, J. T. S. Irvine, *J. Mater. Chem. A* **2019**, 7, 15812.
- [155] W. Liang, S. K. Megarajan, F. Liang, Y. Zhang, G. He, Z. Liu, H. Jiang, *Chem. Eng. J.* **2016**, 305, 176.
- [156] K. Zhang, G. Zhang, Z. Liu, J. Zhu, N. Zhu, W. Jin, *J. Membr. Sci.* **2014**, 471, 9.
- [157] K. Zhang, L. Liu, J. Sunarso, H. Yu, V. Pareek, S. Liu, *Energy Fuels* **2014**, 28, 349.
- [158] C. Zhang, W. Jin, C. Yang, N. Xu, *Catal. Today* **2009**, 148, 298.
- [159] S. Song, P. Zhang, X. Zhang, M. Han, *Int. J. Hydrogen Energy* **2015**, 40, 10894.
- [160] S. Zhang, T. Li, B. Wang, Z. Zhou, X. Meng, N. Yang, X. Zhu, S. Liu, *J. Membr. Sci.* **2022**, 659, 120772.
- [161] S. Zhang, S. Wang, Y. Jin, J. Song, X. Meng, B. Meng, N. Yang, X. Tan, Z. Zhu, S. Liu, *Chem. Eng. J.* **2021**, 419, 129462.
- [162] Z. Wang, Z. Li, Y. Cui, T. Chen, J. Hu, S. Kawi, *Environ. Sci. Technol.* **2019**, 53, 9937.
- [163] W. Liang, H. Zhou, J. Caro, H. Jiang, *Int. J. Hydrogen Energy* **2018**, 43, 14478.
- [164] Z. Shen, P. Lu, J. Hu, X. Hu, *Catal. Commun.* **2010**, 11, 892.
- [165] Q. Li, X. Zhu, Y. He, W. Yang, *Catal. Today* **2010**, 149, 185.
- [166] H. Luo, Y. Wei, H. Jiang, W. Yuan, Y. Lv, J. Caro, H. Wang, *J. Membr. Sci.* **2010**, 350, 154.
- [167] A. Kawahara, Y. Takahashi, Y. Hirano, M. Hirano, T. Ishihara, *Solid State Ionics* **2011**, 190, 53.
- [168] H. Cheng, X. Lu, D. Hu, Y. Zhang, W. Ding, H. Zhao, *Int. J. Hydrogen Energy* **2011**, 36, 528.
- [169] J. Kniep, Y. Lin, *Ind. Eng. Chem. Res.* **2011**, 50, 7941.
- [170] Y. Zhang, J. Liu, W. Ding, X. Lu, *Fuel* **2011**, 90, 324.
- [171] H. Jiang, Z. Cao, S. Schirrmeister, T. Schiestel, J. Caro, *Angew. Chem., Int. Ed.* **2010**, 49, 5656.
- [172] B. Meng, H. Zhang, J. Qin, X. Tan, R. Ran, S. Liu, *Sep. Purif. Technol.* **2015**, 147, 406.
- [173] Z. Cao, H. Jiang, H. Luo, S. Baumann, W. A. Meulenber, H. Voss, J. Caro, *Catal. Today* **2012**, 193, 2.
- [174] J. Garcia-Fayos, M. P. Lobera, M. Balaguer, J. M. Serra, *Front. Mater.* **2018**, 5, 31.
- [175] S. Bhatia, C. Y. Thien, A. R. Mohamed, *Chem. Eng. J.* **2009**, 148, 525.
- [176] O. Czuprat, T. Schiestel, H. Voss, J. Caro, *Ind. Eng. Chem. Res.* **2010**, 49, 10230.



Young-il Kwon is currently a Ph.D. candidate in advanced material engineering at Chungbuk National University. He received his Master of Engineering degree from Chungbuk National University, Republic of Korea, in 2018. His research focuses on the design, manufacture, and performance evaluation of ceramic materials with electronic and ionic conductivity for energy devices such as oxygen transport membranes, solid oxide fuel cells, and solid oxide electrolysis cells.



Gyeong Duk Nam received his B.S. and M.S. degrees in advanced material engineering from Chungbuk National University, Republic of Korea, in 2018 and 2020, respectively. He is currently pursuing Ph.D. under the supervision of Prof. Jong Hoon Joo at School of Earth Sciences and Environmental Engineering, Gwangju Institute of Science and Technology. His current research interests are the evaluation of ceramic materials with oxygen ion or proton conductivity and their application including oxygen transport membrane and proton-conducting solid oxide fuel/electrolysis cells.



Gahyeon Lee received her B.S. and M.S. degrees in advanced material engineering from Chungbuk National University, Republic of Korea, in 2020 and 2022, respectively. She is currently a Ph.D. candidate in the School of Earth Sciences and Environmental Engineering, Gwangju Institute of Science and Technology under the supervision of Prof. Jong Hoon Joo. Her current research focuses on ceramic materials with ion conductivity for solid oxide electrolysis cells (SOEC) and catalyst materials for electrochemical water splitting.



Soomin Choi received her bachelor's degree in advanced material engineering from Chungbuk National University, Republic of Korea, in 2021. As a graduate student, her research focuses on energy materials based on electrochemistry analysis at the School of Earth Sciences and Environmental Engineering, Gwangju Institute of Science and Technology.



Jong Hoon Joo received his Ph.D. degree in materials science and engineering from Pohang University of Science and Technology in 2008. From 2009 to 2012, he was a postdoctoral research scientist (Alexander von Humboldt Fellow) at Max-Planck Institute. From 2012 to 2015, he was a senior researcher at Korea Institute of Energy Research. He worked as an associate professor at Chungbuk National University from 2015 to 2021. He joined School of Earth Sciences and Environmental Engineering at Gwangju Institute of Science and Technology as an associate professor in 2021. His research interests are in the development of advanced energy and environmental devices, including next-generation solid oxide fuel cells, hydrogen production using alkaline electrolysis/solid oxide electrolysis cell, CO₂ recycling using electrolysis and methane reaction, electrolyte for solid-state battery, and applications of defect chemistry of ceramic.